



# Construction double electric field of sulphur vacancies as medium ZnS/Bi<sub>2</sub>S<sub>3</sub>-PVDF self-supported recoverable piezoelectric film photocatalyst for enhanced photocatalytic performance

Meng Li, Jingxue Sun <sup>\*</sup>, Gang Chen <sup>\*</sup>, Shunyu Yao, Bowen Cong

MIIT Key Laboratory of Critical Materials Technology for New Energy Conversion and Storage, School of Chemistry and Chemical Engineering, Harbin Institute of Technology, Harbin 150001, PR China

## ARTICLE INFO

### Keywords:

Polarized electric field  
Built-in electric field  
S vacancies  
Reversibility  
COMSOL simulation

## ABSTRACT

When internally polarized by mechanical energy, piezoelectric materials can establish polarization electric field and provide driving force for separating photogenerated carriers. Herein, S vacancies are introduced as an intermediate to make metal ions form coordination bond with F<sup>-</sup> on PVDF (polyvinylidene fluoride) surface, and the built-in electric field is intimately related to polarized electric field. We successfully synthesized ZnS/Bi<sub>2</sub>S<sub>3</sub>-PVDF film photocatalyst containing S vacancies (ZnS-V<sub>S</sub>/Bi<sub>2</sub>S<sub>3</sub>-PVDF). Polarized electric field on PVDF caused by ultrasonic cavitation and built-in electric field formed between ZnS-V<sub>S</sub>/Bi<sub>2</sub>S<sub>3</sub> heterojunction structure are beneficial to interfacial charge transferring. Theoretical calculation simulation demonstrate that the synergistic effect of the double electric fields is propitious to inhibit the recombination of carriers. The hydrogen evolution rate of ZnS-V<sub>S</sub>/Bi<sub>2</sub>S<sub>3</sub>-PVDF reaches 10.07 mmol h<sup>-1</sup>g<sup>-1</sup>. Moreover, it has excellent reversibility and facile recovery capacity. This work provides new platform for photocatalytic reduction of hydrogen evolution and is expected to contribute to clean energy production.

## 1. Introduction

In recent years, with the rapid growth of population and the rapid development of social economy, the increasing demand for energy and the worsening environmental pollution have become two major problems [1–3]. Semiconductor photocatalysis technology has reveal great potential in environmental remediation and clean energy, hence it has attracted extensive attention and become one of the most popular academic issues in recent years [4–6].

Zinc sulfide (ZnS) is a promising semiconductor photocatalyst. It has high activity under ultraviolet light, but has no response under visible light [7,8]. At the same time, it is vulnerable to photocorrosion and electron cavitation composite, which limits its application in the field of photocatalysis [9,10]. Therefore, researchers carry out engineering strategies such as doping, coupling with semiconductors and introducing defect structures to solve the problem of easy recombination of electrons and holes in photocatalysts [11,12]. Jiang et al. constructed a strongly coupled heterojunction photocatalyst consisting of ZnS and Bi<sub>2</sub>S<sub>3</sub>. The interface of heterostructure makes carrier separation and transport effective [13]. Hao et al. constructed ZnS/g-C<sub>3</sub>N<sub>4</sub>

heterostructure, which cause the built-in electric field between ZnS and C<sub>3</sub>N<sub>4</sub>. So as to improve the photoinduced electron-hole separation capability [14]. Up to now, there are many reports about the heterojunction between ZnS nanoparticles and other semiconductors to form a built-in electric field, thus inhibiting the recombination of carriers. However, the interfacial electric field formed by the heterojunction structure has little intensity, narrow action range, weak driving force, and limited effect on the separation of photoelectric carriers. In order to solve the problem that the carrier is easy to recombination from the photocatalyst itself, introducing vacancies into photocatalyst can narrow the band gap to a certain extent, so as to achieve the purpose of expanding light absorption. At the same time, the introduction of vacancies makes it easier to capture photogenerated electrons, thus inhibiting the recombination of photogenerated electrons and holes. Nevertheless, introducing heterojunction structure and vacancy into photocatalysis has not fundamentally solved the problem of easy recombination of carriers, so it is urgent to find a reasonable way to effectively separate carriers.

Recently, constructing space electric field is an valid pattern to promote carrier separation [15]. However, it is rare to introduce the

<sup>\*</sup> Corresponding authors.

E-mail addresses: [jxsun@hit.edu.cn](mailto:jxsun@hit.edu.cn) (J. Sun), [gchen@hit.edu.cn](mailto:gchen@hit.edu.cn) (G. Chen).



polarized electric field as driving force to effectively enhance the separation of carriers [16–18]. Piezoelectric materials capable of forming polarized electric fields have non-centrosymmetric structure [19]. The positive and negative charge centers of piezoelectric materials noncoincidence under the mechanical deformation or applied electric field, thus generating piezoelectric potential [20–22]. The piezoelectric potential can modulate the charge at the heterojunction and Schottky junction interface of photocatalyst to provide driving force for the separation carriers [23–25]. Typical piezoelectric materials include ZnO, CdS, MoS<sub>2</sub>, BaTiO<sub>3</sub>, etc [26–29]. But these inorganic piezoelectric materials are fragile, which greatly restrict their practical applications [30–32]. However, polymer piezoelectric materials have excellent flexibility, non-toxicity, high chemical stability and high piezoelectric coefficient, such as polyvinylidene fluoride (PVDF), polyvinyl fluoride (PVF), polyvinyl chloride (PVC) [33–35]. Yin et al. exploited PVDF to inhibit the recombination of photogenerated electrons and holes in MoS<sub>2</sub>/g-C<sub>3</sub>N<sub>4</sub> heterojunction photocatalyst to enhance photocatalytic performance [36]. Introducing piezoelectric effect into photocatalytic reaction is an effective way to inhibit recombination of carriers. However, simple recombination fails to fully connect the piezoelectric effect and the heterojunction structure to achieve the optimal synergistic effect.

In this work, we have designed hybrid ZnS-V<sub>S</sub>/Bi<sub>2</sub>S<sub>3</sub>-PVDF recoverable self-supporting flexible film photocatalyst combined with PVDF and semiconductor materials. The introduction of S vacancies makes F exposed by PVDF film occupy S vacancies and form Zn-F coordination bond. The S vacancies are used as a link to fully combine the built-in electric field with the polarized electric field. ZnS-V<sub>S</sub> and Bi<sub>2</sub>S<sub>3</sub> construct a heterojunction structure to form a built-in electric field, which effectively separates electrons and holes. Meanwhile, as flexible polymer piezoelectric material, PVDF is deformed under the action of ultrasonic waves, resulting in macroscopic polarization. Therefore, the polarized electric field formed at the interface between ZnS-V<sub>S</sub>/Bi<sub>2</sub>S<sub>3</sub> and PVDF is regarded as the driving force of carrier directional migration. The synergistic effect of double electric fields is conducive to improve carrier mobility and reduce recombination probability. This research work offers a new idea for the design of other high activity photocatalytic systems.

## 2. Experimental

### 2.1. Materials

Zinc chloride (ZnCl<sub>2</sub>), bismuth nitrate pentahydrate (Bi(NO<sub>3</sub>)<sub>3</sub>·5H<sub>2</sub>O), sodium sulfate (Na<sub>2</sub>SO<sub>4</sub>), sodium sulphide nonahydrate (Na<sub>2</sub>S·9H<sub>2</sub>O), sodium sulfite (Na<sub>2</sub>SO<sub>3</sub>), thiourea, polyvinylidene fluoride (PVDF) were bought from Aladdin Chemical Co., Ltd.

### 2.2. Hydrothermal synthesis of ZnS-V<sub>S</sub> and ZnS

5 mmol ZnCl<sub>2</sub> and 5 mmol thiourea were added to 30 mL of ethanol solution. After about 30 min stirring, the clear solution was transferred to 50 mL Teflon-line stainless steel autoclave and heated at 160 °C for 12 h. The obtained precipitate was centrifuged, and washed with distilled water and ethanol for three times. Finally the trapped power was dried at 60 °C overnight. Pure ZnS was prepared by the same procedure mentioned above in the condition of changing thiourea to 9 mmol.

### 2.3. Hydrothermal synthesis of ZnS/Bi<sub>2</sub>S<sub>3</sub> and ZnS-V<sub>S</sub>/Bi<sub>2</sub>S<sub>3</sub>

The above 0.3 g ZnS-V<sub>S</sub>, 0.032 mmol Bi(NO<sub>3</sub>)<sub>3</sub>·5H<sub>2</sub>O and 0.56 mmol thiourea were added into 25 mL of ethanol, continuous stirring for 30 min. Then, the clear solution was transferred to 50 mL Teflon-line stainless steel autoclave and heated at 180 °C for 24 h. The obtained ZnS-V<sub>S</sub>/Bi<sub>2</sub>S<sub>3</sub> precipitate was centrifuged, and washed with distilled

water and ethanol for three times. Finally the trapped power was dried at 60 °C overnight. The synthesis of ZnS/Bi<sub>2</sub>S<sub>3</sub> remains other conditions remain consistent, and ZnS-V<sub>S</sub> nanoparticles are replaced by ZnS.

### 2.4. Preparation of ZnS-V<sub>S</sub>/Bi<sub>2</sub>S<sub>3</sub>-PVDF film

0.5 g PVDF powder was completely dissolved in 5 mL DMF after continuous stirring for 2 h. Subsequently, the uniform transparent solution was formed. Then 0.5 g ZnS-V<sub>S</sub>/Bi<sub>2</sub>S<sub>3</sub> powder was added, and stir the solution vigorously for 1 h. After that, the obtained mixture was coated on glass slide with drop-coating. Finally, the coated product was cured in vacuum oven at 60 °C manufacture ZnS-V<sub>S</sub>/Bi<sub>2</sub>S<sub>3</sub>-PVDF film.

### 2.5. Characterizations

The X-ray diffraction (XRD) on a Rigaku D/max-2000 diffractometer with Cu K $\alpha$  radiation. X-ray photoelectron spectroscopy (XPS) was applied Thermo Scientific ESCALAB 250Xi X-ray photoelectron spectrometer by energy of 20 eV and Al K $\alpha$  excitation source. Transmission electron microscope (TEM) and high resolution TEM (HRTEM) were performed on FEI Tecnai G2 S-Twin operating at 300 kV. The UV-vis spectrum of the product was received by spectrophotometer (HITACHI UH-4150). The photoluminescence (PL) spectrum was gained by HORIBA FluoroMax-4. In the presence of external pressure on the thin film photocatalyst, and named as ZnS-V<sub>S</sub>/Bi<sub>2</sub>S<sub>3</sub>-PVDF-p (presence pressure). Pressure-free photocatalyst film was named ZnS-V<sub>S</sub>/Bi<sub>2</sub>S<sub>3</sub>-PVDF-a (absence pressure).

### 2.6. Photocatalytic performance test

Generally, the above-mentioned ZnS-V<sub>S</sub>/Bi<sub>2</sub>S<sub>3</sub>-PVDF film was placed in 45 mL of an aqueous solution containing 1.0 M Na<sub>2</sub>S and 1.0 M Na<sub>2</sub>SO<sub>3</sub> with continuous ultrasonic. The photocatalytic system was vacuumized three to clean remove the air before using the 300 W Xe lamp (PLS-SXE300D, Beijing Perfectlight). The temperature of the reaction vessel was maintained at 6 °C throughout the photocatalytic hydrogen evolution. The hydrogen content was monitored by gas chromatograph (Agilent 780A GC). The whole photocatalytic process was carried out under ultrasonic conditions. In order to prevent ultrasonic overheating, it is necessary to add ice bags into the ultrasonic machine and constantly change the water in the machine. The AQY is calculated as the formula: [13].

$$AQY = \frac{N_e}{N_p} \times \% = \frac{2 \times M \times N_A \times h \times c}{S \times P \times t \times \lambda} \quad (1)$$

where  $N_e$  is the number of electrons in the reaction,  $N_p$  is the incident photons,  $N_A$  is Avogadro constant,  $M$  is the number of molecules of H<sub>2</sub>,  $c$  is the speed of light,  $h$  is the Planck constant,  $P$  is light intensity,  $S$  is the illumination area,  $t$  is the photoreaction time and  $\lambda$  is the wavelength of different incident light.

### 2.7. Photoelectrochemical test

The photoelectrochemical measurements were carried out on an electrochemical workstation with three-electrode system (CHI660C), Pt and Ag/AgCl as counter electrode and reference electrode. Xe lamp of 300 W ( $\lambda \geq 420$  nm) was used as light source, meanwhile, the 0.5 M Na<sub>2</sub>SO<sub>3</sub> aqueous solution was served as electrolyte.

## 3. Results and discussion

### 3.1. Morphology and structure characterization

The manufacturing route of ZnS-V<sub>S</sub>/Bi<sub>2</sub>S<sub>3</sub>-PVDF film is shown in Fig. 1a. Firstly, ZnS-V<sub>S</sub>/Bi<sub>2</sub>S<sub>3</sub> nanoparticles are synthesized by typical

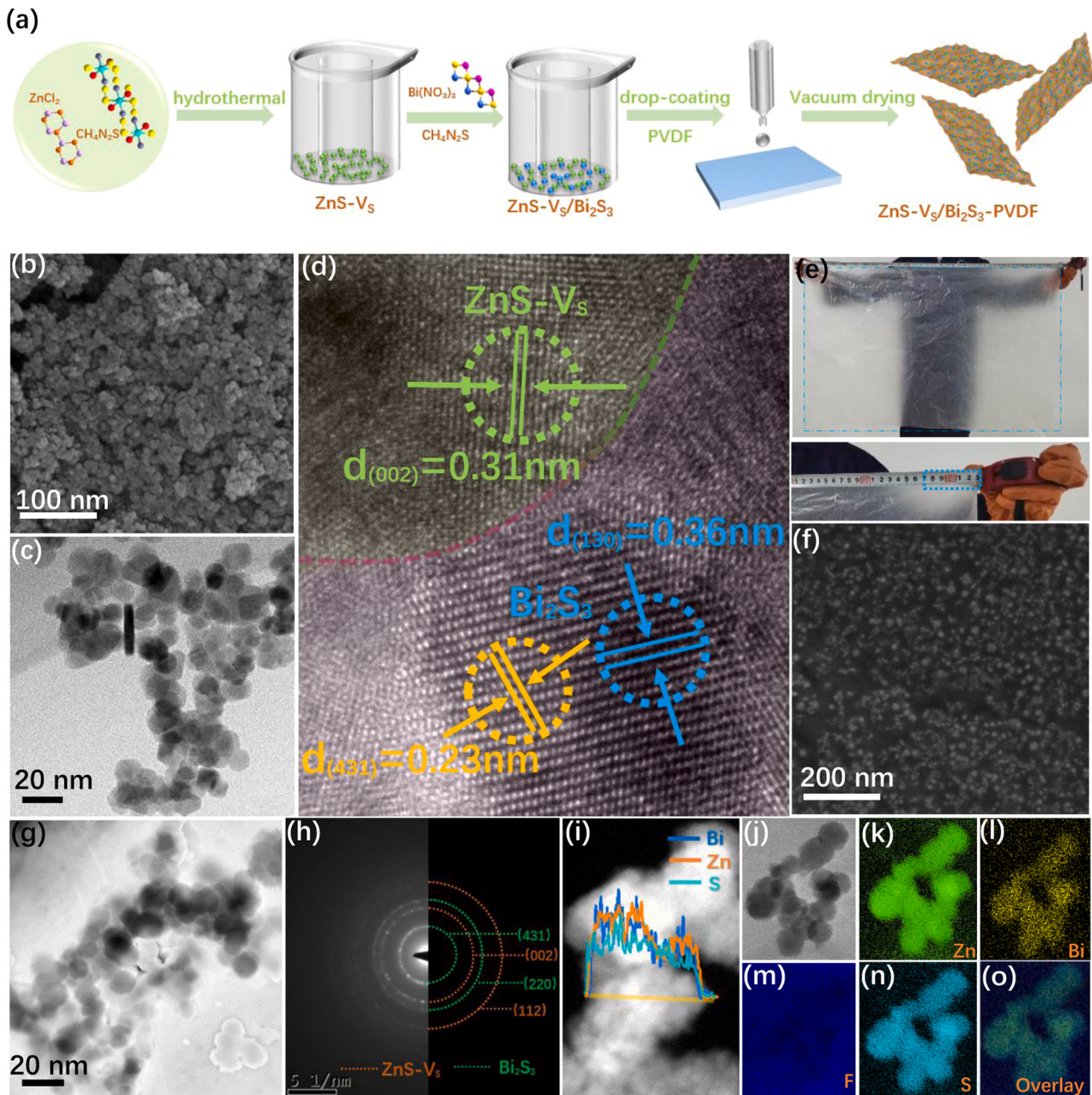


**Fig. 1.** (a) Schematic diagram of the fabrication process of ZnS-V<sub>s</sub>/Bi<sub>2</sub>S<sub>3</sub>-PVDF. (b, c) SEM and TEM images of ZnS-V<sub>s</sub>/Bi<sub>2</sub>S<sub>3</sub> nanoparticles. (d) HRTEM image of ZnS-V<sub>s</sub>/Bi<sub>2</sub>S<sub>3</sub>. (e) Photograph of ZnS-V<sub>s</sub>/Bi<sub>2</sub>S<sub>3</sub>-PVDF film. (f, g) SEM and TEM images of ZnS-V<sub>s</sub>/Bi<sub>2</sub>S<sub>3</sub>-PVDF. (h) SAED patterns of ZnS-V<sub>s</sub>/Bi<sub>2</sub>S<sub>3</sub>. (i) Line scanning profile of ZnS-V<sub>s</sub>/Bi<sub>2</sub>S<sub>3</sub>. (j-o) HAADF-STEM image of ZnS-V<sub>s</sub>/Bi<sub>2</sub>S<sub>3</sub>-PVDF and elemental mapping of Zn, Bi, S, F and overlay.

hydrothermal method. Subsequently, the ZnS-V<sub>s</sub>/Bi<sub>2</sub>S<sub>3</sub>-PVDF flexible film is prepared through spin coating process. The morphology and microstructure of ZnS-V<sub>s</sub>/Bi<sub>2</sub>S<sub>3</sub> are researched by SEM and TEM images. The morphology of the exposed ZnS-V<sub>s</sub>/Bi<sub>2</sub>S<sub>3</sub> is approximately regular microspheres with diameter of about 20 nm (Fig. 1b and c). HRTEM image further suggests that ZnS nanoparticles are closely connected to Bi<sub>2</sub>S<sub>3</sub>, forming compact interface between ZnS and Bi<sub>2</sub>S<sub>3</sub> in the hybrid photocatalyst (Fig. 1d). Lattice fringe with lattice spacing of 0.31 nm can be labeled to (002) crystal planes of ZnS [37,38]. Meanwhile, the fringe spacing are 0.36 nm and 0.23 nm, which are exactly consistent with the (130) and (431) lattice plane of Bi<sub>2</sub>S<sub>3</sub> [39]. As shown in Fig. S1a and S1b, the atoms in the yellow region are fuzzy and discontinuous, indicating that it is a region rich in S defects. The reason of S vacancies is that thiourea can not be completely translate into S<sup>2-</sup> for chemical reaction. This will cause the problem of insufficient S source content, which

makes it impossible to form a face-centered cubic structure around Zn<sup>2+</sup> in the form of four coordination. Therefore, S vacancies will appear in the crystal structure. The ZnS-V<sub>s</sub>/Bi<sub>2</sub>S<sub>3</sub>-PVDF film with an area of 113 cm × 90 cm is prepared as illustrated in Fig. 1e. Its strong mechanical properties make it a promising photocatalyst. Simultaneously, it can be recovered from water without any time-consuming treatment. As shown in Fig. 1f and g, SEM and TEM images are applied to further observe the surface structure of ZnS-V<sub>s</sub>/Bi<sub>2</sub>S<sub>3</sub>-PVDF film. ZnS and Bi<sub>2</sub>S<sub>3</sub> nanoparticles are embedded in the flat PVDF film, and the size and morphology of nanoparticles are not affected by the film formation. The selected area electron diffraction (SAED) diagram shows a clear diffraction ring, indicating the high crystallinity of ZnS-V<sub>s</sub>/Bi<sub>2</sub>S<sub>3</sub>. The diffraction ring in Fig. 1h demonstrate the existence of (002), (112) crystal planes of ZnS-V<sub>s</sub> and (220), (431) crystal planes of Bi<sub>2</sub>S<sub>3</sub>. These diffraction rings are attributed to the polycrystalline property of the

ZnS-V<sub>S</sub>/Bi<sub>2</sub>S<sub>3</sub> nanoparticles. The linear scanning curve in Fig. 1i shows the existence of Zn, Bi and S elements in ZnS-V<sub>S</sub>/Bi<sub>2</sub>S<sub>3</sub> composite photocatalyst. Furthermore, the element mapping pattern clearly demonstrates that Zn, Bi, S and F exist in ZnS-V<sub>S</sub>/Bi<sub>2</sub>S<sub>3</sub>-PVDF film photocatalyst, and F element is located in the whole region (Fig. 1j-o). The above results indicate that ZnS-V<sub>S</sub>/Bi<sub>2</sub>S<sub>3</sub>-PVDF film photocatalyst has been successfully synthesized.

As shown in Fig. 2a, the pure PVDF film shows a X-ray characteristic diffraction peak at  $2\theta = 18.4^\circ$ , which indicates that PVDF film mainly forms  $\beta$  phase. Similar diffraction peaks can be observed from ZnS-V<sub>S</sub>/Bi<sub>2</sub>S<sub>3</sub>-PVDF film. This shows that the addition of ZnS and Bi<sub>2</sub>S<sub>3</sub> has little effect on the crystalline phase of PVDF film. It is obvious that the crystallinity of  $\beta$  phase in ZnS-V<sub>S</sub>/Bi<sub>2</sub>S<sub>3</sub>-PVDF film is better than that of naked PVDF. This is mainly due to the Zn-F coordination bond between F<sup>-</sup> exposed in PVDF and ZnS-V<sub>S</sub>, which enhances the interface effect. It is more conducive to the formation of  $\beta$  phase [40]. All the peaks of samples are perfectly matched with ZnS (PDF#03-0524) and Bi<sub>2</sub>S<sub>3</sub> (PDF#06-0333). Compared with ZnS/Bi<sub>2</sub>S<sub>3</sub>, the (002) diffraction peak position of ZnS-V<sub>S</sub>/Bi<sub>2</sub>S<sub>3</sub> gradually moves to a higher angle. The results show that the lattice in ZnS-V<sub>S</sub>/Bi<sub>2</sub>S<sub>3</sub> structure has changed. The interlayer stacking distance decreases slightly and the interlayer stacking density increases, which proves that there is a certain S vacancies. Moreover, it is concluded that ZnS nanoparticle is cubic and Bi<sub>2</sub>S<sub>3</sub> nanoparticle is orthorhombic.

The surface chemical composition and state of the prepared samples are investigated by XPS. In Fig. 2b, the XPS spectrum of Zn 2p in ZnS/Bi<sub>2</sub>S<sub>3</sub> has two peaks at 1021.6 eV and 1045.5 eV, which are classified as Zn 2p<sub>1/2</sub> and Zn 2p<sub>3/2</sub>. This indicates that the Zn element exists in the form of Zn<sup>2+</sup> [41,42]. In addition, the binding energy of Zn 2p in ZnS-V<sub>S</sub>/Bi<sub>2</sub>S<sub>3</sub> photocatalyst gradually decreased. This result is attributed to S vacancies in the ZnS structure. The binding energies of Zn 2p<sub>1/2</sub> and Zn 2p<sub>3/2</sub> moved 1.52 eV towards the lower binding energies. We can reasonably infer that these peaks of Zn<sup>2+</sup> are close to the S vacancies of single negative charge state. This leads to an increase in the electron density near the S vacancies and decrease in the binding energy of Zn<sup>2+</sup>. The binding energies of 158.2 eV and 163.9 eV are easily classified to Bi 4f<sub>7/2</sub> and Bi 4f<sub>5/2</sub> of Bi<sub>2</sub>S<sub>3</sub>. The S 2p of XPS spectra (Fig. 2c) appeared at

160.7 eV and 161.8 eV, completely consistent with the previously reported binding energies of S 2p<sub>3/2</sub> and S 2p<sub>1/2</sub> [43]. The above results show that the valence of Bi element in Bi<sub>2</sub>S<sub>3</sub> nanocomposites is mainly + 3, and the valence of S element is - 2 [44].

It can be observed from Fig. 2c that the binding energy of Bi 4f of ZnS-V<sub>S</sub>/Bi<sub>2</sub>S<sub>3</sub> is higher than that of ZnS/Bi<sub>2</sub>S<sub>3</sub>, which is due to the difference of surface electron density. It has been reported that the change of binding energy is related to the difference of surface electron density. It is caused by electron transfer between semiconductors with different Fermi energy, electrons will transition from high energy level to low energy level [45]. Compared with the ZnS-V<sub>S</sub>/Bi<sub>2</sub>S<sub>3</sub> hybridization process, electrons are more inclined to transfer from Bi<sub>2</sub>S<sub>3</sub> to ZnS-V<sub>S</sub>. Therefore, the electron concentration in Bi<sub>2</sub>S<sub>3</sub> decreases, and eventually the binding energy of Bi 4f is increased [46]. Meanwhile, the peak area of S in ZnS-V<sub>S</sub>/Bi<sub>2</sub>S<sub>3</sub> is lower than that in ZnS/Bi<sub>2</sub>S<sub>3</sub>, which further indicates the existence of S vacancies in the ZnS structure. The XPS peak at 685.3 eV is attributed to the existence of Zn-F coordination bond (Fig. 2d). The illustration clearly shows the structure diagram of Zn-F coordination bond formed by F<sup>-</sup> on PVDF surface occupying S vacancy in ZnS. Furthermore, the valence band (VB) of the sample is determined by the XPS spectrum in Fig. S3. The VB of ZnS and ZnS-V<sub>S</sub> are 2.84 eV (relative to the Fermi level), the VB of Bi<sub>2</sub>S<sub>3</sub> is 0.94 eV.

Fourier transform infrared spectroscopy (FTIR) is used to analyze the structure of PVDF and ZnS-V<sub>S</sub>/Bi<sub>2</sub>S<sub>3</sub>-PVDF. Fig. 2e reveals the FTIR of PVDF and ZnS-V<sub>S</sub>/Bi<sub>2</sub>S<sub>3</sub>-PVDF films. The absorption bands at 602 cm<sup>-1</sup>, 680 cm<sup>-1</sup>, 868 cm<sup>-1</sup> and 1403 cm<sup>-1</sup> represent the  $\beta$  crystalline phase in PVDF [47]. The absorption band at 836 cm<sup>-1</sup> corresponds to the C-C bond rocking vibration in PVDF [48]. Meanwhile, the absorption peak near 1166 cm<sup>-1</sup> is attributed to the tensile vibration of C-H [49]. Compared with ZnS-V<sub>S</sub>/Bi<sub>2</sub>S<sub>3</sub>-PVDF films, the absorption peak frequency and band shape of PVDF are basically the same, which manifest that the functional groups of PVDF have not changed substantially. However, the intensity of some absorption peaks has changed. The absorption peaks at 1065 cm<sup>-1</sup> is considered to be the tensile vibration of C-F. The strength of ZnS-V<sub>S</sub>/Bi<sub>2</sub>S<sub>3</sub>-PVDF film is weakened, indicating that the interaction between F atoms and C atoms is weakened [50]. The trend of absorption peak intensity indicates that Zn<sup>2+</sup> can form

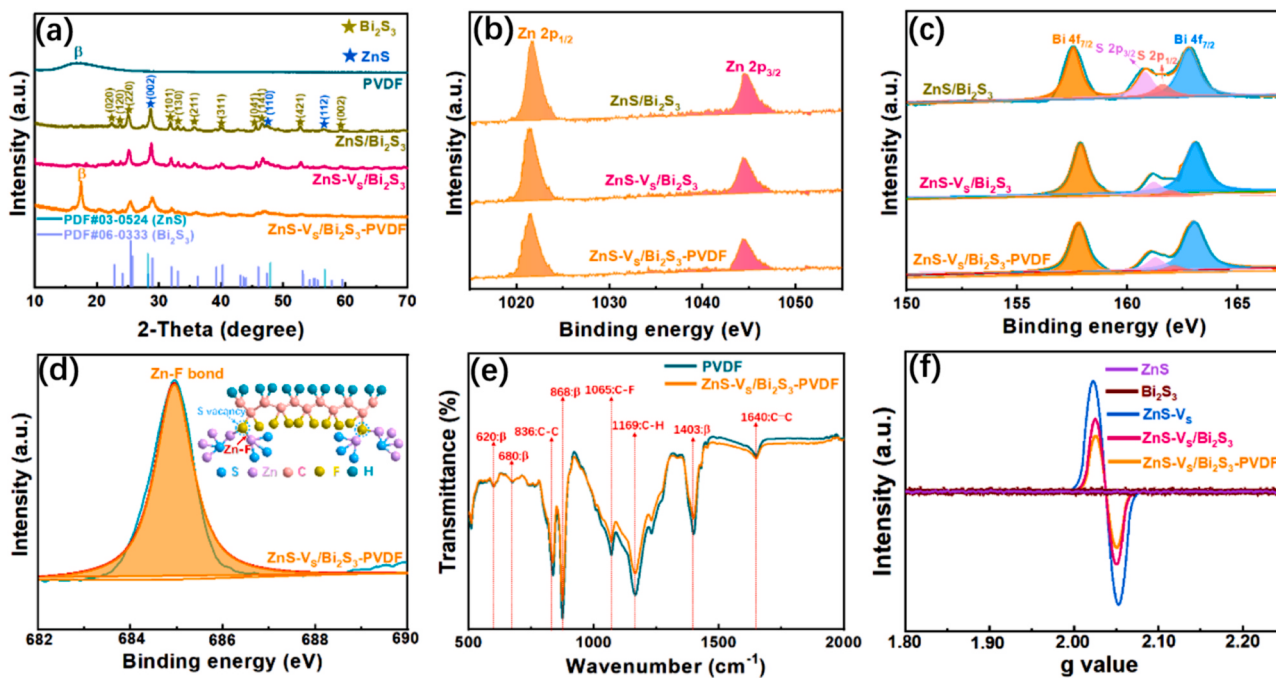


Fig. 2. (a) XRD pattern of PVDF, ZnS-V<sub>S</sub>, ZnS/Bi<sub>2</sub>S<sub>3</sub>, ZnS-V<sub>S</sub>/Bi<sub>2</sub>S<sub>3</sub> and ZnS-V<sub>S</sub>/Bi<sub>2</sub>S<sub>3</sub>-PVDF. XPS spectra of ZnS/Bi<sub>2</sub>S<sub>3</sub>, ZnS-V<sub>S</sub>/Bi<sub>2</sub>S<sub>3</sub> and ZnS-V<sub>S</sub>/Bi<sub>2</sub>S<sub>3</sub>-PVDF nanocomposite: (b) Zn 2p, (c) Bi 4f and S 2p. (d) F 1s of ZnS-V<sub>S</sub>/Bi<sub>2</sub>S<sub>3</sub>-PVDF (The illustration is a schematic diagram of Zn-F coordination bond formed by PVDF and ZnS-V<sub>S</sub>). (e) FTIR spectra of PVDF film and ZnS-V<sub>S</sub>/Bi<sub>2</sub>S<sub>3</sub>-PVDF films. (f) EPR spectra of ZnS, ZnS-V<sub>S</sub>, Bi<sub>2</sub>S<sub>3</sub>, ZnS-V<sub>S</sub>/Bi<sub>2</sub>S<sub>3</sub> and ZnS-V<sub>S</sub>/Bi<sub>2</sub>S<sub>3</sub>-PVDF.

coordination covalent bond with F. Due to the induction of  $Zn^{2+}$ , the vibration coupling of C—F bond is weakened. Therefore, the absorption peaks of C—F are reduced, while the absorption peaks of C=C and C—H are enhanced [51]. The change of absorption peak at  $1640\text{ cm}^{-1}$  corresponds to the absorption peak of C=C. The formation of Zn—F bond leads to partial defluorination of PVDF, the content of C=C in ZnS-V<sub>S</sub>/Bi<sub>2</sub>S<sub>3</sub>-PVDF film increases to some extent [48]. Above all, it is proved that Zn-F coordination bond exists in ZnS-V<sub>S</sub>/Bi<sub>2</sub>S<sub>3</sub>-PVDF.

Fig. 2f shows the EPR spectra of different samples.  $g = 2.003$  is the electronic paramagnetic resonance signal. There is no obvious characteristic peak in ZnS at  $g = 2.003$ , but there is an obvious characteristic peak in ZnS-V<sub>S</sub>, which indicates that ZnS with S vacancies has been successfully synthesized [52]. ZnS-V<sub>S</sub>/Bi<sub>2</sub>S<sub>3</sub> also has characteristic peaks, however its intensity is lower than ZnS-V<sub>S</sub>. This indicates that some S vacancies are filled in the process of compounding Bi<sub>2</sub>S<sub>3</sub>. The EPR signal of ZnS-V<sub>S</sub>/Bi<sub>2</sub>S<sub>3</sub>-PVDF is lower than that of ZnS-V<sub>S</sub>/Bi<sub>2</sub>S<sub>3</sub>. The possible reason is that the exposed F in PVDF film occupies the position of S vacancies and forms Zn-F coordination bond, which makes the S vacancies occupied by filling to some extent.

### 3.2. Piezoelectric characterization

Piezoresponse force microscopy (PFM) is a significant measure to characterize the microcosmic domain structure of ferroelectric materials [53]. The strength of piezoelectric response can be expressed by the vibration amplitude and phase at the same position of the membrane. A sharp contrast can be observed in the piezoelectric response amplitude diagram (Fig. 3a). The phase image in Fig. 3b has  $180^\circ$  domains, which indicates that ZnS-V<sub>S</sub>/Bi<sub>2</sub>S<sub>3</sub>-PVDF film shows excellent piezoelectricity in a certain polarization direction. Moreover, in order to further verify

the piezoelectric performance, the piezoelectric hysteresis curve and butterfly curve are measured in Fig. 3c and d. The apparent butterfly curve and distinct square phase curve indicate that ZnS-V<sub>S</sub>/Bi<sub>2</sub>S<sub>3</sub>-PVDF film has piezoelectric characteristics and polarization response conversion behaviors. When the applied voltage is reversed from  $+10\text{ V}$  to  $-10\text{ V}$ , the phase reversal of ZnS-V<sub>S</sub>/Bi<sub>2</sub>S<sub>3</sub>-PVDF film approaches  $180^\circ$ . The results show that ZnS-V<sub>S</sub>/Bi<sub>2</sub>S<sub>3</sub>-PVDF film has favorable piezoelectric properties.

### 3.3. Photochemical and electrochemical characterization

The optical properties of ZnS, ZnS/Bi<sub>2</sub>S<sub>3</sub>, ZnS-V<sub>S</sub>/Bi<sub>2</sub>S<sub>3</sub>, ZnS-V<sub>S</sub>/Bi<sub>2</sub>S<sub>3</sub>-PVDF are probed through UV-vis diffuse reflectance spectra. As shown in Fig. 4a, compared with pure ZnS, the absorption edge of the ZnS/Bi<sub>2</sub>S<sub>3</sub> composite appear red shift from  $510\text{ nm}$  to  $615\text{ nm}$ . The consequence reveal that the ZnS/Bi<sub>2</sub>S<sub>3</sub> heterojunction composite can make victorious utilize of sunlight, thus it is expected to improve the photocatalytic performance. At the same time, compared with ZnS/Bi<sub>2</sub>S<sub>3</sub> photocatalyst, ZnS-V<sub>S</sub>/Bi<sub>2</sub>S<sub>3</sub> sample exhibit more apparent visible light absorption intensity and expanded absorption edge. The results explain that the existence of S vacancies is conducive to enhance light absorption ability. There is no significant transform between the absorption edges of ZnS-V<sub>S</sub>/Bi<sub>2</sub>S<sub>3</sub> and ZnS-V<sub>S</sub>/Bi<sub>2</sub>S<sub>3</sub>-PVDF, indicating that PVDF has insubstantial appliance for enhancing the absorption of visible light. Simultaneously, the band structure of the ZnS, ZnS-V<sub>S</sub> and Bi<sub>2</sub>S<sub>3</sub> corresponding to the visible region (Fig. S2 and S4) are calculated by the altered Kubelka-Munk function ( $a\hbar\nu = A(\hbar\nu - E_g)$ , in which  $\hbar\nu$  is the photon energy,  $E_g$  is the band gap,  $A$  is the constant). The  $E_g$  values of ZnS, ZnS-V<sub>S</sub> and Bi<sub>2</sub>S<sub>3</sub> are  $3.47\text{ eV}$ ,  $3.38\text{ eV}$  and  $1.77\text{ eV}$ .

The surface photovoltage (SPV) signal in Fig. 4b determines the

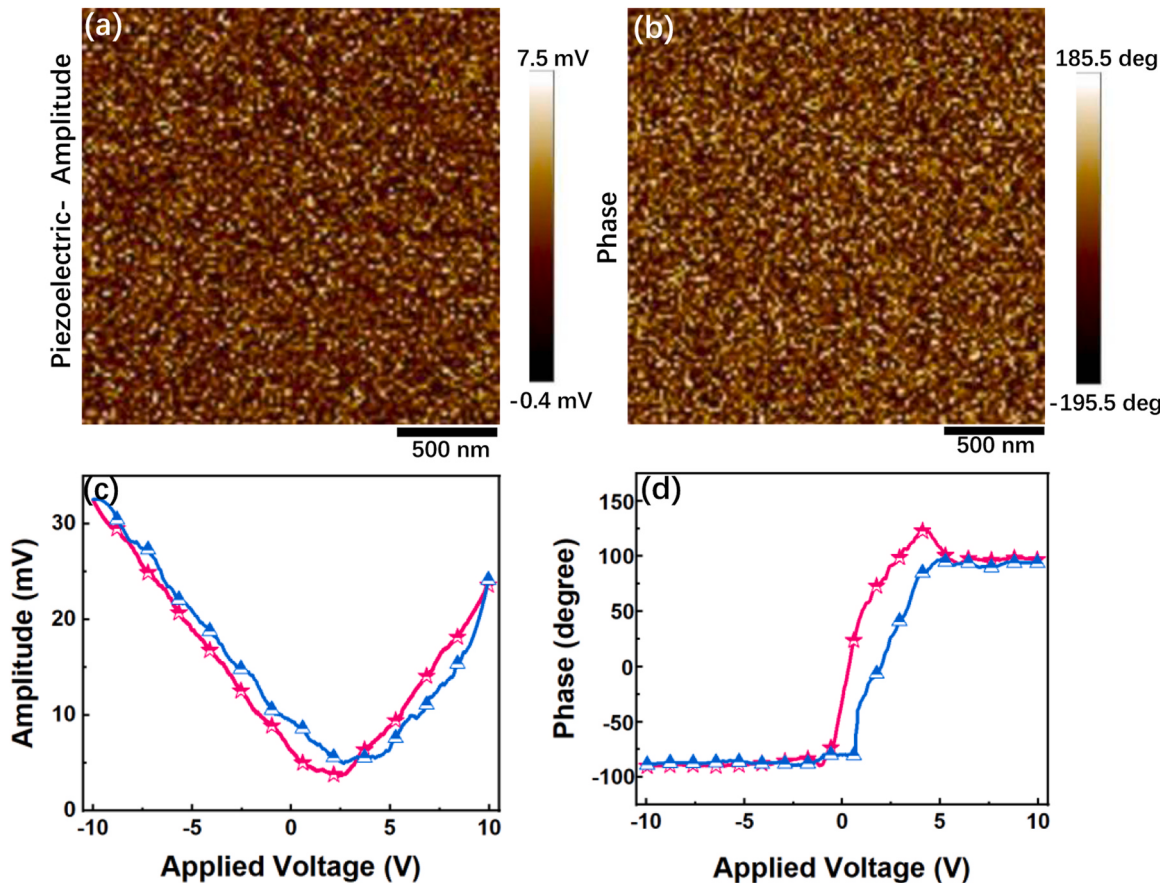
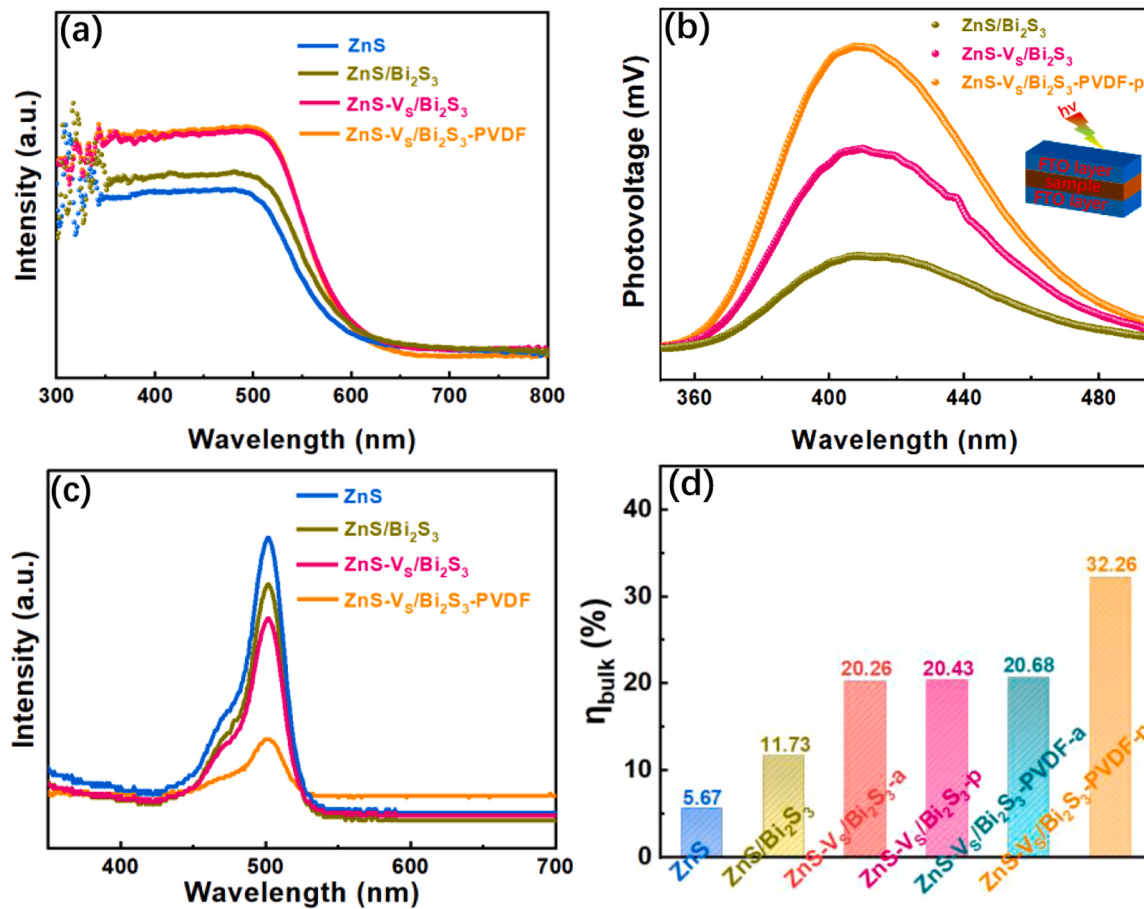


Fig. 3. (a) PFM piezoelectric amplitude and (b) phase images of ZnS-V<sub>S</sub>/Bi<sub>2</sub>S<sub>3</sub>-PVDF film. (c) butterfly loops and (d) piezoelectric hysteresis of ZnS-V<sub>S</sub>/Bi<sub>2</sub>S<sub>3</sub>-PVDF film.



**Fig. 4.** (a) UV-vis diffuse reflection spectrum of ZnS, ZnS/Bi<sub>2</sub>S<sub>3</sub>, ZnS-V<sub>s</sub>/Bi<sub>2</sub>S<sub>3</sub> and ZnS-V<sub>s</sub>/Bi<sub>2</sub>S<sub>3</sub>-PVDF. (b) Surface photovoltage (c) The PL spectra of ZnS, ZnS/Bi<sub>2</sub>S<sub>3</sub>, ZnS-V<sub>s</sub>/Bi<sub>2</sub>S<sub>3</sub>, ZnS-V<sub>s</sub>/Bi<sub>2</sub>S<sub>3</sub>-PVDF. (d) bulk-charge separation efficiency ( $\eta_{\text{bulk}}$ ) of different photocatalysts.

carrier migration behavior [55]. The SPV signal of ZnS-V<sub>s</sub>/Bi<sub>2</sub>S<sub>3</sub>-PVDF-p is higher than that of other samples, which can be attributed to two reasons. One reason is ZnS-V<sub>s</sub>/Bi<sub>2</sub>S<sub>3</sub> constructs heterojunction structure to form an internal electric field. It can accelerate the separation of light-induced carriers and the migration of electrons on the interface of heterogeneous structures. The other reason is the polarization electric field constructed by the piezoelectric effect of PVDF to enhance the separation of carriers. The synergistic effect of double electric fields reduces the recombination probability of carriers in ZnS-V<sub>s</sub>/Bi<sub>2</sub>S<sub>3</sub>-PVDF-p thin film photocatalyst. As plotted in Fig. 4c, ZnS photocatalyst display strong PL peak, which illustrated that more carriers are formed and reassembled rapidly. The internal electric field formed between heterojunctions can effectively promote the carrier separation, which makes the PL intensity of ZnS/Bi<sub>2</sub>S<sub>3</sub> decrease obviously. The PL intensity of ZnS-V<sub>s</sub>/Bi<sub>2</sub>S<sub>3</sub> is further reduced, which revealed that the existence of S vacancy can significantly improve the lifetime of carriers. The PL strength of ZnS-V<sub>s</sub>/Bi<sub>2</sub>S<sub>3</sub>-PVDF films is significantly reduced after deformation. This is due to the piezoelectric polarization electric field induced by the macroscopic polarization of PVDF film to some extent.

The Zeta potential is applied to characterize the amount of charge on the surface of particles. The Zeta potential of ZnS-V<sub>s</sub>/Bi<sub>2</sub>S<sub>3</sub>-PVDF-p is  $-37.45 \text{ mV}$ , while the ZnS, ZnS/Bi<sub>2</sub>S<sub>3</sub>, ZnS-V<sub>s</sub>/Bi<sub>2</sub>S<sub>3</sub>-a, ZnS-V<sub>s</sub>/Bi<sub>2</sub>S<sub>3</sub>-p and ZnS-V<sub>s</sub>/Bi<sub>2</sub>S<sub>3</sub>-PVDF-a are  $-10.83 \text{ mV}$ ,  $-18.16 \text{ mV}$ ,  $-27.69 \text{ mV}$ ,  $-27.83 \text{ mV}$  and  $-28.41 \text{ mV}$ , respectively (Fig. S5). Compared with ZnS-V<sub>s</sub>/Bi<sub>2</sub>S<sub>3</sub>-p, the Zeta potential of ZnS-V<sub>s</sub>/Bi<sub>2</sub>S<sub>3</sub>-PVDF-a is almost the same, which further proves that the change of ZnS-V<sub>s</sub>/Bi<sub>2</sub>S<sub>3</sub>-PVDF-p Zeta potential is caused by the piezoelectric effect produced by PVDF rather than ultrasound effect. The Zeta potential of ZnS-V<sub>s</sub>/Bi<sub>2</sub>S<sub>3</sub>-PVDF-

has changed compared with ZnS-V<sub>s</sub>/Bi<sub>2</sub>S<sub>3</sub>-a. The reason for the potential reduction of ZnS-V<sub>s</sub>/Bi<sub>2</sub>S<sub>3</sub> is that nanoparticles are partially embedded in PVDF film. The PVDF film itself also has a certain charge, these two factors together leads to tiny improvement in the potential of ZnS-V<sub>s</sub>/Bi<sub>2</sub>S<sub>3</sub>-PVDF-a. ZnS-V<sub>s</sub>/Bi<sub>2</sub>S<sub>3</sub>-PVDF-p has the highest Zeta potential, illustration that it has the strongest electric field. It is conducive to improving the separation and transmission of charge.

Quantitative measurements of bulk-charge separation efficiency ( $\eta_{\text{bulk}}$ ) for different photocatalysts are made using the formula reported by Kim and colleagues [54]. The  $\eta_{\text{bulk}}$  of ZnS, ZnS/Bi<sub>2</sub>S<sub>3</sub>, ZnS-V<sub>s</sub>/Bi<sub>2</sub>S<sub>3</sub>-a, ZnS-V<sub>s</sub>/Bi<sub>2</sub>S<sub>3</sub>-p, ZnS-V<sub>s</sub>/Bi<sub>2</sub>S<sub>3</sub>-PVDF-a and ZnS-V<sub>s</sub>/Bi<sub>2</sub>S<sub>3</sub>-PVDF-p are estimated to be  $\approx 5.67\%$ ,  $\approx 11.73\%$ ,  $\approx 20.26\%$ ,  $\approx 20.43\%$ ,  $\approx 20.68\%$  and  $\approx 32.26\%$ , respectively. This high  $\eta_{\text{bulk}}$  indicates that the carrier separation is more distinct, so that more electrons have the opportunity to participate in the photocatalytic hydrogen evolution reaction (Fig. 4d).

The linear scanning voltammetry (LSV) curves in Fig. 5a illustrate the charge transfer kinetics of the sample. S vacancy in ZnS-V<sub>s</sub>/Bi<sub>2</sub>S<sub>3</sub> can capture photogenerated electrons, which makes the hydrogen evolution potential of ZnS-V<sub>s</sub>/Bi<sub>2</sub>S<sub>3</sub> composite is lower than that of ZnS/Bi<sub>2</sub>S<sub>3</sub>. Thereby improving the charge density and carrier separation efficiency. External pressure is applied to ZnS-V<sub>s</sub>/Bi<sub>2</sub>S<sub>3</sub>-PVDF thin films to randomly orient the dipoles in PVDF. Thus, the charge transfer at the interface between semiconductor and PVDF thin films is facilitated, and the hydrogen evolution potential is reduced. Simultaneously, the Tafel slope of ZnS-V<sub>s</sub>/Bi<sub>2</sub>S<sub>3</sub>-PVDF-p ( $195 \text{ mV}\cdot\text{dec}^{-1}$ ) is smaller than that of ZnS-V<sub>s</sub>/Bi<sub>2</sub>S<sub>3</sub> ( $227 \text{ mV}\cdot\text{dec}^{-1}$ ) and ZnS/Bi<sub>2</sub>S<sub>3</sub> ( $283 \text{ mV}\cdot\text{dec}^{-1}$ ). The above results reveal that ZnS-V<sub>s</sub>/Bi<sub>2</sub>S<sub>3</sub>-PVDF-p has excellent efficiency in the photocatalytic hydrogen evolution reaction.

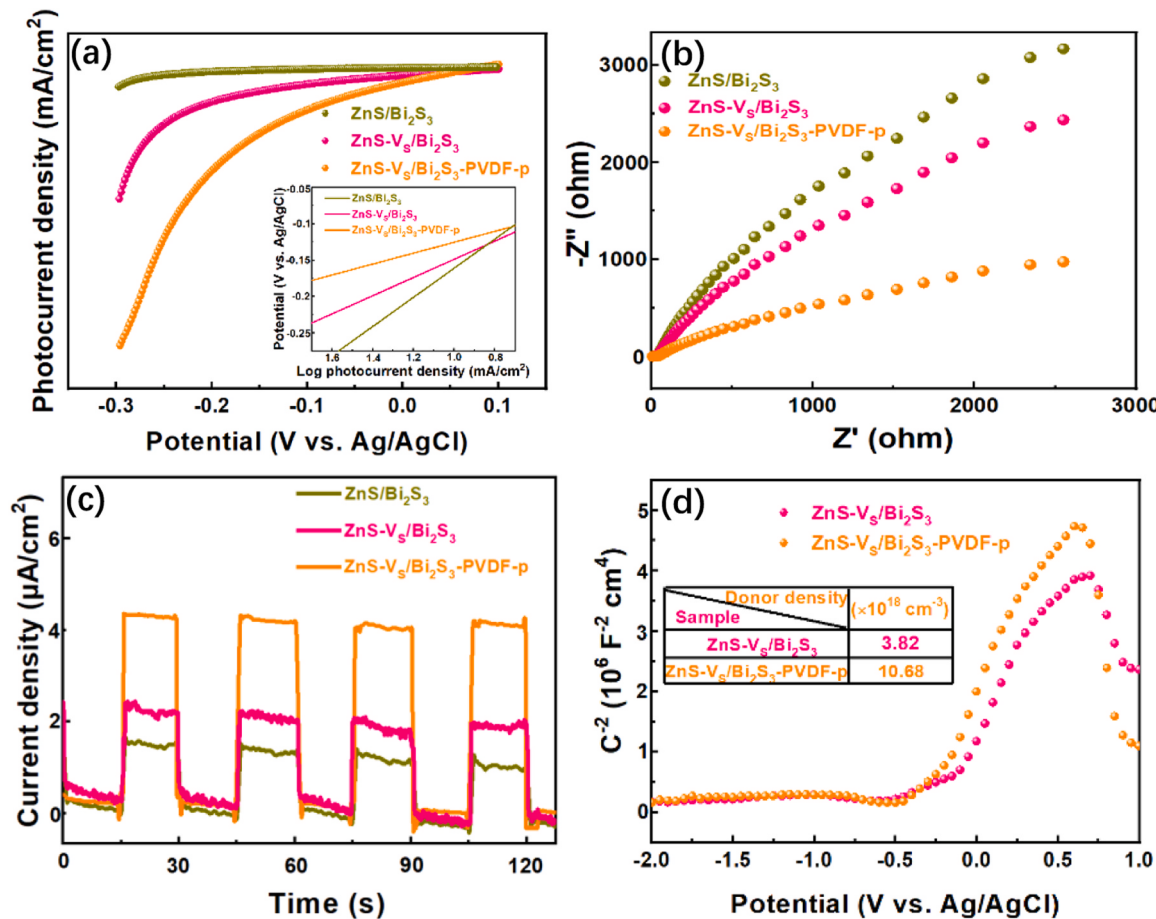


**Fig. 5.** (a) LSV curves (The insert is Tafel slopes). (b) EIS Nyquist plots, (c) transient photocurrent responses of ZnS/Bi<sub>2</sub>S<sub>3</sub>, ZnS-V<sub>s</sub>/Bi<sub>2</sub>S<sub>3</sub> and ZnS-V<sub>s</sub>/Bi<sub>2</sub>S<sub>3</sub>-PVDF-p. (d) Mott-Schottky curves of ZnS-V<sub>s</sub>/Bi<sub>2</sub>S<sub>3</sub> and ZnS-V<sub>s</sub>/Bi<sub>2</sub>S<sub>3</sub>-PVDF-p. The insert in Fig. 5d is parameter calculated by Mott-Schottky plots.

The EIS Nyquist diagram in Fig. 5b shows that the semi-circular arc represents the charge transfer process. The smaller arc radius of ZnS-V<sub>s</sub>/Bi<sub>2</sub>S<sub>3</sub>-PVDF-p proves that charge carriers can move smoothly with less impulse. In addition, the transient photocurrent response under the irradiation of excited light is shown in Fig. 5c. It can be seen that the photocurrent increases rapidly with the switching on of light, indicating the generation of photogenerated electrons and holes. As the light is taken away, the photocurrent rapidly drops down zero due to the quick recombination of electron-hole pairs. The transient photocurrent of ZnS-V<sub>s</sub>/Bi<sub>2</sub>S<sub>3</sub>-PVDF-p photocatalyst is much higher than that of other samples. These results once again prove that well-designed photocatalyst is helpful for charge separation. When the piezoelectric electric field is applied, the carriers in the piezoelectric copolymer will drift [56]. Positive piezoelectric charges attract electrons in semiconductor and negative electric charges attract holes in semiconductor. Thereby effectively separating electrons and holes in the semiconductor [57].

The pivotal parameters in the Mott-Schottky curve are devoted to calculate the carriers concentration of the photocatalyst, according to formula: [58].

$$N_D = - \left\{ \frac{2}{e\epsilon_0} \right\} \left\{ \frac{d(1/C^2)}{dE} \right\}^{-1} \quad (2)$$

$e$  is the unit charge,  $\epsilon_0$  is the vacuum permittivity,  $\epsilon$  is the relative permittivity,  $C$  is the space charges capacitance of the semiconductor,  $N_D$  is the carriers concentration,  $E$  is the electrode potential, respectively. Fig. 5d demonstrates the change of carriers concentration of ZnS-V<sub>s</sub>/Bi<sub>2</sub>S<sub>3</sub> and ZnS-V<sub>s</sub>/Bi<sub>2</sub>S<sub>3</sub>-PVDF-p under piezoelectric potential. When external pressure is applied to ZnS-V<sub>s</sub>/Bi<sub>2</sub>S<sub>3</sub>, the electron concentration

increases from  $3.83 \times 10^{18} \text{ cm}^{-3}$  to  $10.68 \times 10^{18} \text{ cm}^{-3}$ . This will result in the accumulation of local positive piezoelectric charges. Thus, the electron-hole pairs produced by light are separated by a piezoelectric potential. So more electrons can participate in the photocatalytic hydrogen production reaction.

#### 3.4. Photocatalytic hydrogen evolution activity

The photocatalytic activity is evaluated by hydrogen production rate of different samples under visible light. The schematic diagram of the photocatalytic reaction device and the reaction process are shown in Fig. S6 and Video S1. Fig. 6a reveals the hydrogen evolution rate by ZnS, ZnS-V<sub>s</sub>, ZnS/Bi<sub>2</sub>S<sub>3</sub>, ZnS-V<sub>s</sub>/Bi<sub>2</sub>S<sub>3</sub>, ZnS-V<sub>s</sub>/Bi<sub>2</sub>S<sub>3</sub>-PVDF-a and ZnS-V<sub>s</sub>/Bi<sub>2</sub>S<sub>3</sub>-PVDF-p within 2.5 h. The hydrogen evolution rate of ZnS-V<sub>s</sub> ( $1.57 \text{ mmol h}^{-1} \text{ g}^{-1}$ ) is 1.69 times that of ZnS nanoparticles ( $0.93 \text{ mmol h}^{-1} \text{ g}^{-1}$ ). This is due to the existence of S vacancy enhances the utilization rate of visible light and as the active site of the reaction, so that its photocatalytic activity is improved. The hydrogen evolution rate of ZnS/Bi<sub>2</sub>S<sub>3</sub> ( $1.77 \text{ mmol h}^{-1} \text{ g}^{-1}$ ) is 1.90 times that of ZnS nanoparticles ( $0.93 \text{ mmol h}^{-1} \text{ g}^{-1}$ ). The reason is that the heterojunction interface between ZnS and Bi<sub>2</sub>S<sub>3</sub> is conducive to the separation of charge carriers. Meanwhile, the hydrogen generation rate of ZnS-V<sub>s</sub>/Bi<sub>2</sub>S<sub>3</sub> ( $4.84 \text{ mmol h}^{-1} \text{ g}^{-1}$ ) is 2.73 times that of ZnS/Bi<sub>2</sub>S<sub>3</sub> ( $1.77 \text{ mmol h}^{-1} \text{ g}^{-1}$ ). The hydrogen production rate of ZnS-V<sub>s</sub>/Bi<sub>2</sub>S<sub>3</sub>-PVDF-a has almost no obvious change compared with that of ZnS-V<sub>s</sub>/Bi<sub>2</sub>S<sub>3</sub>. In the absence of pressure, PVDF has no contribution to the separation and transfer of carriers. Under ultrasonic excitation, the rate of hydrogen production of ZnS-V<sub>s</sub>/Bi<sub>2</sub>S<sub>3</sub>-PVDF-p can reach  $10.07 \text{ mmol h}^{-1} \text{ g}^{-1}$ . The external mechanical force causes PVDF to generate polarized electric field, which

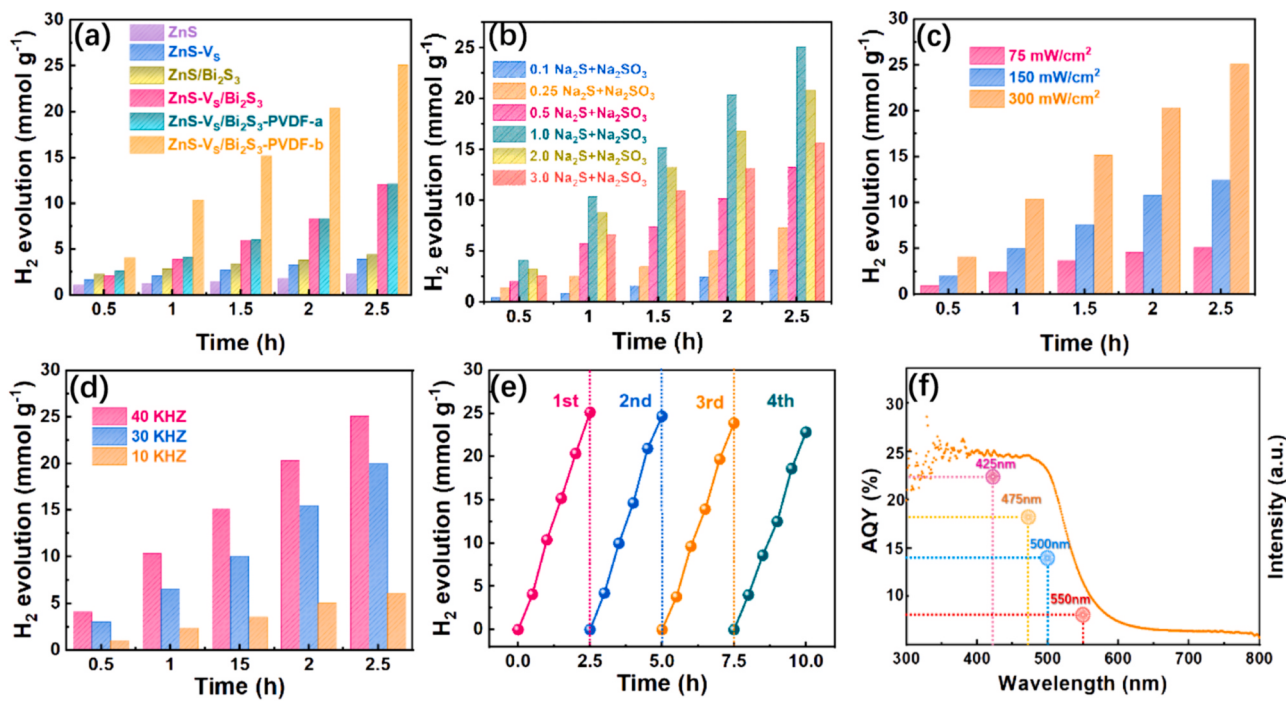


**Fig. 6.** Hydrogen evolution rate of (a) different photocatalysts, (b) different concentrations of sacrificial agent, (c) different optical power density, (d) different ultrasonic intensity. (e) Cyclic stability of  $\text{ZnS-V}_\text{S}/\text{Bi}_2\text{S}_3$ -PVDF-p under Xe lamp. (f) The apparent quantum yield of  $\text{ZnS-V}_\text{S}/\text{Bi}_2\text{S}_3$ -PVDF-p under different monochromatic light illumination.

effectively controls the carrier migration direction and separation efficiency.

Supplementary material related to this article can be found online at doi:10.1016/j.apcatb.2021.120792.

In order to investigate the influence of external mechanical pressure on the photocatalyst performance, the pressure is applied by stirring (Fig. S7). It is found that the hydrogen production rate of  $\text{ZnS-V}_\text{S}/\text{Bi}_2\text{S}_3$ -PVDF-p is also obviously affected, which shows that the piezoelectric effect of PVDF under ultrasound is the most prominent. At the same time, the influence of different rotational speeds on hydrogen production rate is examined. The greater the rotational speed, the greater the pressure exerted on PVDF, resulting in the stronger piezoelectric effect. The hydrogen production rate is  $4.43 \text{ mmol h}^{-1}\text{g}^{-1}$  at 200 rpm and  $6.19 \text{ mmol h}^{-1}\text{g}^{-1}$  at 800 rpm. Table S1 shows the hydrogen production activity of metal sulfide photocatalysts in recent literature, and our work has excellent photocatalytic hydrogen production rate. Table S2 compares the hydrogen production efficiency of  $\text{ZnS-V}_\text{S}/\text{Bi}_2\text{S}_3$ -PVDF-p with other piezoelectric photocatalysts. The results show that the synergistic effect of polarized electric field and built-in electric field are conducive to carrier separation and improve photocatalytic activity.

The hydrogen evolution rate is positively correlated with the sacrificial agent concentration. The sacrificial agent can trap the holes and make the electrons and holes separated effectively [59]. As shown in Fig. 6b, when the concentration of the sacrificial agent is  $1.0 \text{ M}$  ( $\text{Na}_2\text{S}+\text{Na}_2\text{SO}_3$ ), the hydrogen production efficiency of  $\text{ZnS-V}_\text{S}/\text{Bi}_2\text{S}_3$ -PVDF-p reaches the maximum value of  $10.07 \text{ mmol h}^{-1}\text{g}^{-1}$ . With the increase of sacrificial agent concentration, the hydrogen evolution of  $\text{ZnS-V}_\text{S}/\text{Bi}_2\text{S}_3$ -PVDF-p decreased. The reason for this phenomenon is that S will be produced during the photocatalytic reaction, and S will cover the appearance of  $\text{ZnS-V}_\text{S}/\text{Bi}_2\text{S}_3$ -PVDF photocatalyst. For one thing, the S coating prevents the incidence of light and reduces the utilization rate of visible light. For another thing, the S layer covers the active sites on the photocatalyst surface, which reduces the photocatalytic hydrogen production efficiency. Fig. 6c shows the correlation between Xe lamp power density and hydrogen generation rate. The higher the power density of the laser,

the more likely it is to excite the electrons participating in the photocatalytic reaction. The Xe lamp power density is  $150 \text{ mW/cm}^2$ , the hydrogen production rate reaches  $4.99 \text{ mmol h}^{-1}\text{g}^{-1}$ . The hydrogen production rate is  $2.03 \text{ mmol h}^{-1}\text{g}^{-1}$  at  $75 \text{ mW/cm}^2$ .

The change of mechanical force will promote the separation of electrons and holes in different degrees. Fig. 6d demonstrate the effect of vibration power on hydrogen production rate. The hydrogen production of mechanical vibration at  $10 \text{ kHz}$  frequency ( $2.42 \text{ mmol h}^{-1}\text{g}^{-1}$ ) is much lower than that at  $40 \text{ kHz}$  vibration power. The performance of  $\text{ZnS-V}_\text{S}/\text{Bi}_2\text{S}_3$ -PVDF-p can be stable and reusable under continuous illumination for more than  $10 \text{ h}$  as shown in Fig. 6e. The film after photocatalytic reaction can be directly recovered from the reaction solution. This indicates that  $\text{ZnS-V}_\text{S}/\text{Bi}_2\text{S}_3$ -PVDF-p has excellent reversibility and effortless recovery (Fig. S8). Moreover, the SEM images of  $\text{ZnS-V}_\text{S}/\text{Bi}_2\text{S}_3$  and  $\text{ZnS-V}_\text{S}/\text{Bi}_2\text{S}_3$ -PVDF after photocatalytic reaction (Fig. S9). Their morphology and size have almost unchanged, which manifest that the  $\text{ZnS-V}_\text{S}/\text{Bi}_2\text{S}_3$  and  $\text{ZnS-V}_\text{S}/\text{Bi}_2\text{S}_3$ -PVDF photocatalyst have high stability. In order to further verify the stability of  $\text{ZnS-V}_\text{S}/\text{Bi}_2\text{S}_3$ -PVDF, the reaction system of  $\text{ZnS-V}_\text{S}/\text{Bi}_2\text{S}_3$ -PVDF is detected by inductively coupled plasma (ICP) method. After four cycles, the concentrations of  $\text{Zn}^{2+}$  and  $\text{Bi}^{3+}$  can be neglected (Fig. S10). In addition, the F concentration is detected by ion chromatography, and the F concentration hardly changed before and after photocatalytic reaction (Table S3). The above results indicate that  $\text{ZnS-V}_\text{S}/\text{Bi}_2\text{S}_3$ -PVDF membrane can exist stably. In order to confirm the uniformity of  $\text{ZnS-V}_\text{S}/\text{Bi}_2\text{S}_3$ -PVDF film, six parts with equal area are cut out on the large area film for photocatalytic hydrogen evolution test. As shown in Fig. S11, the photocatalytic hydrogen evolution efficiency of the six parts are almost equal, which indicates the uniformity of  $\text{ZnS-V}_\text{S}/\text{Bi}_2\text{S}_3$ -PVDF membrane.

The apparent quantum yield (AQY) associated with the wavelength of  $\text{ZnS-V}_\text{S}/\text{Bi}_2\text{S}_3$ -PVDF-p exposed to different monochromatic light is shown in Fig. 6f. The AQY of  $\text{ZnS-V}_\text{S}/\text{Bi}_2\text{S}_3$ -PVDF-p can reach  $23.6\%$  at the wavelength of  $425 \text{ nm}$ . This is similar to the trend of UV-vis spectrum. Meanwhile, as shown in Fig. S12, the AQY of  $\text{ZnS-V}_\text{S}/\text{Bi}_2\text{S}_3$ -PVDF-p ( $25.8\%$ ) under visible light irradiation is  $2.18$  times that of  $\text{ZnS}/\text{Bi}_2\text{S}_3$

(11.8%). Table S4 shows the AQY of metal sulfide photocatalysts in recent literature, and our work has excellent AQY. This is attributed to the synergistic effect of polarized electric field and built-in electric field by ZnS-V<sub>S</sub>/Bi<sub>2</sub>S<sub>3</sub>-PVDF film. Thereby promoting the charge separation, accelerating the carrier migration rate and prolonging the carrier life.

### 3.5. Simulation theoretical calculation

So as to probe the correlation between pressure action and piezoelectric potential, we utilized COMSOL Multiphysics 5.4 to simulate calculation. Fig. 7 explores the change of PVDF piezoelectric potential under different pressures. The simulated dimension of the PVDF film is  $20 \times 150 \times 1 \text{ nm}^3$ . The polar axis of the simulated PVDF membrane is oriented along the z axis. Other parameters used in simulation, such as elastic matrix, coupling matrix, and relative permittivity of PVDF can be used as predetermined parameters in COMSOL Multiphysics 5.4. The consequence received from this is that the piezoelectric potential in the PVDF film is continuously distributed along the polar axis. When PVDF is subjected to ultrasonic wave, positive and negative potential will be generated on the opposite side. In addition, the potential value increases continuously, because the larger the proportion of polarization plane. The resulting piezoelectric potential and piezoelectric current are greater. The piezoelectric potential of PVDF under  $10^3 \text{ Pa}$  pressure is 180 mV. When the bubble with cavitation effect caused by ultrasonic wave breaks, the impact force on the catalyst can reach up to  $10^8 \text{ Pa}$  and the maximum piezoelectric potential is 1.38 V. Therefore, in the process of piezoelectric photocatalysis, the piezoelectric polarization electric field caused by ultrasonic activation promotes the orderly migration of carriers. This leads to a high photoelectric conversion process of the ZnS-V<sub>S</sub>/Bi<sub>2</sub>S<sub>3</sub>-PVDF compound.

In order to further explore the effect of S vacancy, theoretical model are established under the framework of density functional theory (DFT). Their electronic properties are studied by first principles calculations. The band gap can be obtained from the electronic structure of Fig. 8a, c and e. Obviously, the band gap of ZnS with S vacancies is smaller than that of ZnS, which is consistent with the results of UV-vis diffuse reflection spectrum. In addition, ZnS with S vacancies exhibits different electronic structures from ZnS. This is due to the contribution of atomic orbitals, indicating that the introduction of S vacancies has a great influence on the electronic properties. At the same time, the more electrons are accumulated in the region where the band structure curve is concentrated. Fig. 8b shows that CB of ZnS-V<sub>S</sub> is mainly composed of Zn 3p and S 3p, while VB consists of Zn 4s and S 3s. The presence of S vacancies in the ZnS crystal structure is more conducive to the transition of electrons from the VB to the CB under radiation, thereby increasing the carrier concentration. The electric field in the space charge region

will increase more conducive to promoting charge separation. Fig. 8d shows that CB of ZnS is composed of Zn 4s, Zn 3d and S 3s orbitals, and VB is Zn 3d and S 3p orbitals. The VB electrons in ZnS are easily excited due to the low degree of hybridization between Zn atoms and adjacent S atoms in VB. However, due to the high density of the hybrid electron cloud near the Zn atoms and S atoms in CB. Therefore, most of the CB electrons are transferred in ZnS, which causes a high degree of recombination of photogenerated carriers. As for Bi<sub>2</sub>S<sub>3</sub>, CB is mainly composed of Bi 6p and S 3s; VB consists of Bi 6p and S 3p orbitals (Fig. 8f). The mixed electron density of Bi atoms and adjacent S atoms is high, which will enhance the electrostatic attraction between the nucleus and electrons. In the ZnS-V<sub>S</sub> and Bi<sub>2</sub>S<sub>3</sub> heterojunction structure, the CB electrons in ZnS-V<sub>S</sub> and the VB of Bi<sub>2</sub>S<sub>3</sub> holes are more active. This may play a decisive role in the charge transfer kinetics in the ZnS-V<sub>S</sub>/Bi<sub>2</sub>S<sub>3</sub> composite. The above results reveal the energy band structure and orbitals of ZnS, ZnS-V<sub>S</sub> and Bi<sub>2</sub>S<sub>3</sub>. This is beneficial to grasp the way of charge migration.

The density functional theory (DFT) are calculated to investigate the charge transfer approach in the heterojunction of ZnS-V<sub>S</sub> and Bi<sub>2</sub>S<sub>3</sub>. As shown in Fig. 8g and h, ZnS-V<sub>S</sub> has low surface work function and weak binding ability to electrons. Hence, it can effectively accelerate photo-generated charge migration and promote surface reaction. As described in Fig. 8h and i, the work function of Bi<sub>2</sub>S<sub>3</sub> (4.52 eV) is smaller than that of ZnS-V<sub>S</sub> (5.27 eV). When the two Fermi levels ( $E_F$ ) are different, the interface electron transfer process will occur between Bi<sub>2</sub>S<sub>3</sub> and ZnS-V<sub>S</sub>. Eventually their  $E_F$  are aligned with the same height. Since semiconductor  $E_F$  is a factor that directly affects the density of clustered electrons, it can be expressed by the following formula: [60,61].

$$E_F = E_{CB} + KT \ln \frac{n_c}{N_c} \quad (3)$$

where  $E_{CB}$  represents the CB energy,  $n_c$  is the cumulative electron density and  $N_c$  is the carrier density of the semiconductor. Specifically, accumulated electrons will be transferred from Bi<sub>2</sub>S<sub>3</sub> to ZnS-V<sub>S</sub> by means of heterojunctions. This charge flow causes a built-in electric field to be formed near the interface, which can effectively control the migration and separation of photogenerated.

### 3.6. Photocatalytic mechanism

PVDF is an excellent polymer piezoelectric film. When it is deformed by external force, the polarization phenomenon will be generated inside. This will cause positive and negative charges present to the two relative surfaces. The spontaneous polarization of PVDF can be generated by mechanical ultrasound. It can effectively convert the external force into electric energy and generate polarization electric field. ZnS-V<sub>S</sub> and Bi<sub>2</sub>S<sub>3</sub>

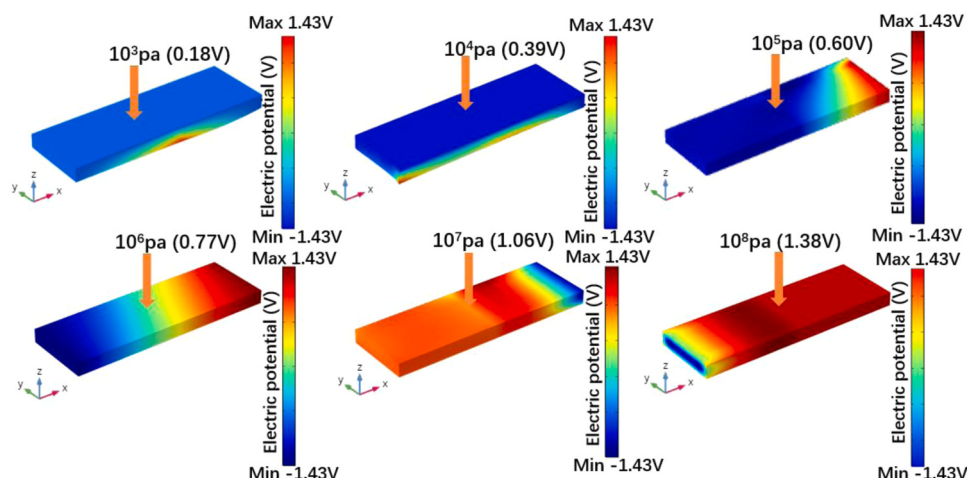
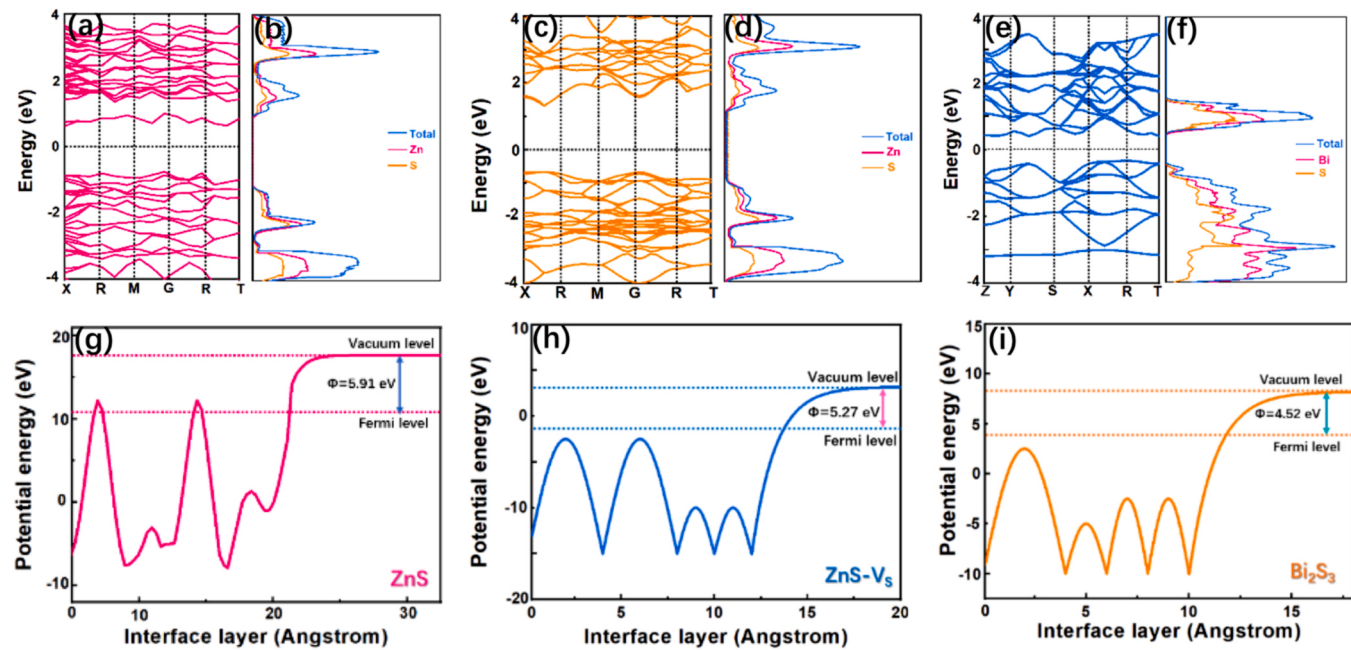


Fig. 7. COMSOL simulates the potential distribution of piezoelectric PVDF films under different pressures.



**Fig. 8.** Energy band structures of (a) ZnS-V<sub>S</sub> (c) ZnS and (e) Bi<sub>2</sub>S<sub>3</sub>. Density of states of (b) ZnS-V<sub>S</sub> (d) ZnS and (f) Bi<sub>2</sub>S<sub>3</sub>. (g, h, i) DFT calculated potential diagrams of ZnS, ZnS-V<sub>S</sub> and Bi<sub>2</sub>S<sub>3</sub> surfaces in vacuum.

are in close contact to form a heterojunction structure. Due to the difference of their Fermi level and carrier concentration, carrier diffusion occurs between ZnS-V<sub>S</sub> and Bi<sub>2</sub>S<sub>3</sub>. Meanwhile, space charge regions are formed on both sides of the interface between ZnS-V<sub>S</sub> and Bi<sub>2</sub>S<sub>3</sub>. Because the interface state is not considered, the charges in space form an internal electric field. The existence of built-in electric field can effectively enhance the separation efficiency of carriers and inhibit charge recombination (Fig. 9a). Introduce S vacancies promotes F<sup>-</sup> on PVDF surface to occupy vacancies in ZnS to form Zn-F coordinate bond, which closely links polarized electric field with built-in electric field (Fig. 9b). The synergistic effect of this double electric field greatly improves the separation of carriers in the semiconductor, and then effectively improves the photocatalytic hydrogen evolution activity.

#### 4. Conclusion

In summary, recoverable ZnS/Bi<sub>2</sub>S<sub>3</sub>-PVDF self-supporting photocatalyst film containing S vacancies are constructed. The synergistic

effect of the built-in electric field generated by ZnS-V<sub>S</sub>/Bi<sub>2</sub>S<sub>3</sub> heterojunction structure and the polarized electric field generated by PVDF are used to accelerate the separation of carriers, thus enhance the photocatalytic hydrogen evolution activity. The introduction of S vacancies makes F ions exposed on PVDF surface form Zn-F bond with Zn ions, which makes the built-in electric field closely integrated with polarized electric field. Meanwhile, the effects of internal electric field and polarized electric field are investigated through DFT calculation and COMSOL simulation. The hydrogen evolution rate of ZnS-V<sub>S</sub>/Bi<sub>2</sub>S<sub>3</sub>-PVDF reaches 10.07 mmol h<sup>-1</sup>g<sup>-1</sup>. Photocatalyst self-supported films still maintain excellent stability after multiple cycles. Its structure has no obvious damage and is facile to recover after photocatalytic reaction. These work provides an innovative way for the construction of efficient photocatalytic system.

#### CRediT authorship contribution statement

Meng Li: Writing – original draft, Conceptualization, Methodology,

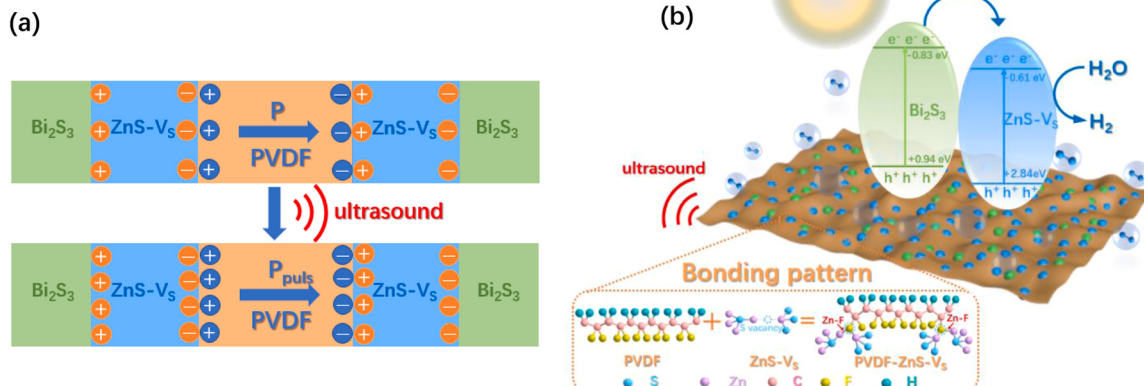


**Fig. 9.** (a) Polarization schematic diagram of PVDF under ultrasonic conditions. (b) Schematic diagram of the photocatalytic mechanism of ZnS-V<sub>S</sub>/Bi<sub>2</sub>S<sub>3</sub>-PVDF under visible light irradiation.

Visualization, Investigation. **Jingxue Sun**: Supervision, Validation, Writing – review & editing, Funding acquisition. **Gang Chen**: Supervision, Validation, Methodology. **Shunyu Yao**: Investigation. **Bowen Cong**: Conceptualization.

## Declaration of Competing Interest

The authors declare that they have no known competing financial interests or personal relationships that could have appeared to influence the work reported in this paper.

## Acknowledgements

This work was financially supported by projects of Natural Science Foundation of China (21471040).

## Appendix A. Supporting information

Supplementary data associated with this article can be found in the online version at [doi:10.1016/j.apcatb.2021.120792](https://doi.org/10.1016/j.apcatb.2021.120792).

## References

- [1] Q. Han, C.B. Wu, H.M. Jiao, R.Y. Xu, Y.Z. Wang, J.J. Xie, Q. Guo, J.W. Tang, Rational design of high-concentration Ti3+ in porous carbon-doped TiO2 nanosheets for efficient photocatalytic ammonia synthesis, *Adv. Mater.* 33 (2021) 2008180–2008189.
- [2] X.B. Li, J. Xiong, X.M. Gao, J. Ma, Z. Chen, B.B. Kang, J.Y. Liu, H. Li, Z.J. Feng, J. T. Huang, Novel BP/BiOBr S-scheme nano-heterojunction for enhanced visible-light photocatalytic tetracycline removal and oxygen evolution activity, *J. Hazard. Mater.* 387 (2020) 11–19.
- [3] J. Dong, Y. Shi, C.P. Huang, Q. Wu, T. Zeng, W.F. Yao, A New and stable Mo-Mo2C modified g-C3N4 photocatalyst for efficient visible light photocatalytic H2 production, *Appl. Catal. B Environ.* 243 (2019) 27–35.
- [4] D.R. Yang, J. Feng, L.L. Jiang, X.L. Wu, L.Z. Sheng, Y.T. Jiang, T. Wei, Z.J. Fan, Photocatalyst interface engineering: spatially confined growth of ZnFe2O4 within graphene networks as excellent visible-light-driven photocatalysts, *Adv. Funct. Mater.* 25 (2015) 7080–7087.
- [5] P.X. Jin, L. Wang, X.L. Ma, R. Lian, J.W. Huang, H.D. She, M.Y. Zhang, Q.Z. Wang, Construction of hierarchical ZnIn2S4@PCN-224 heterojunction for boosting photocatalytic performance in hydrogen production and degradation of tetracycline hydrochloride, *Appl. Catal. B Environ.* 284 (2021) 119762–119770.
- [6] L.Q. Jing, Y.G. Xu, S.Q. Huang, M. Xie, M.Q. He, H. Xu, H.M. Li, Q. Zhang, Novel magnetic CoFe2O4/Ag/Ag3VO4 composites: highly efficient visible light photocatalytic and antibacterial activity, *Appl. Catal. B Environ.* 199 (2016) 11–22.
- [7] C.B. Wu, G.H. Yu, Y. Yin, Y.Z. Wang, L. Chen, Q. Han, J.W. Tang, B. Wang, Mesoporous polymeric cyanamide-triazole-heptazine photocatalysts for highly-efficient water splitting, *Small* 16 (2020) 2003162–2003171.
- [8] G.Q. Han, Y.H. Jin, R.A. Burgess, N.E. Dickenson, X.M. Cao, Y.J. Sun, Visible-light-driven valorization of biomass intermediates integrated with H2 production catalyzed by ultrathin Ni/CdS nanosheets, *J. Am. Chem. Soc.* 139 (2017) 15584–15587.
- [9] M. Li, J.X. Sun, B.W. Cong, S.Y. Yao, G. Chen, Sulphur vacancies modified Cd0.5Zn0.5S/Bi2S3: engineering localized surface plasma resonance enhanced visible light driven hydrogen evolution, *Chem. Eng. J.* 415 (2021) 128868–128873.
- [10] J.F. Liu, P. Wang, J.J. Fan, H.G. Yu, J.G. Yu, In situ synthesis of Mo2C nanoparticles on graphene nanosheets for enhanced photocatalytic H2 production activity of TiO2, *ACS Sustain. Chem. Eng.* 9 (2021) 3821–3830.
- [11] X.M. Xu, L.J. Meng, J. Luo, M. Zhang, Y.T. Wang, Y.X. Dai, C. Sun, Z.Y. Wang, S. G. Yang, H. He, S.B. Wang, Self-assembled ultrathin CoO/Bi quantum dots/defective Bi2MoO6 hollow Z-scheme heterojunction for visible light-driven degradation of diazinon in water matrix: intermediate toxicity and photocatalytic mechanism, *Appl. Catal. B Environ.* 293 (2021) 120231–120239.
- [12] J.G. Hao, W. Li, J.W. Zhai, H. Chen, Progress in high-strain perovskite piezoelectric ceramics, *Mater. Sci. Eng. R Rep.* 135 (2019) 1–57.
- [13] H. Jiang, Z.P. Xing, Z.Z. Li, K. Pan, Z.K. Yang, K. Wang, M.J. Guo, S.L. Yang, W. Zhou, Wide-spectrum response urchin-like Bi2S3 spheres and ZnS quantum dots co-decorated mesoporous g-C3N4 nanosheets heterojunctions for promoting charge separation and enhancing photothermal-photocatalytic performance, *Appl. Surf. Sci.* 527 (2020) 1038–1043.
- [14] X.Q. Hao, J. Zhou, Z.W. Cui, Y.C. Wang, Y. Wang, Z.G. Zou, Zn-vacancy mediated electron-hole separation in ZnS/g-C3N4 heterojunction for efficient visible-light photocatalytic hydrogen production, *Appl. Catal. B Environ.* 229 (2018) 41–51.
- [15] S. Chandrasekaran, L. Yao, L.B. Deng, C. Bowen, Y. Zhang, S.M. Chen, Z.Q. Lin, F. Peng, P.X. Zhang, Recent advances in metal sulfides: from controlled fabrication to electrocatalytic, photocatalytic and photoelectrochemical water splitting and beyond, *Chem. Soc. Rev.* 48 (2019) 4178–4280.
- [16] T. Hisatomi, J. Kubota, K. Domen, Recent advances in semiconductors for photocatalytic and photoelectrochemical water splitting, *Chem. Soc. Rev.* 43 (2014) 7520–7535.
- [17] F. Chen, H.W. Huang, L. Guo, Y.H. Zhang, T.Y. Ma, The role of polarization in photocatalysis, *Angew. Chem. Int. Ed.* 58 (2019) 10061–10073.
- [18] L.P. Zhou, S.Q. Dai, S. Xu, Y.Q. She, Y.L. Li, S. Leveneur, Y.L. Qin, Piezoelectric effect synergistically enhances the performance of Ti32-oxo-cluster/BaTiO3/CuS p-n heterojunction photocatalytic degradation of pollutants, *Appl. Catal. B Environ.* 291 (2021) 120019–120030.
- [19] L. Wang, S. Liu, Z. Wang, Y. Zhou, Y. Qin, Z.L. Wang, Piezotronic effect enhanced photocatalysis in strained anisotropic ZnO/TiO2 nanoplatelets via thermal stress, *ACS Nano* 10 (2016) 2636–2643.
- [20] S.A. Han, T.H. Kim, S.K. Kim, K.H. Lee, H.J. Park, J.H. Lee, S.W. Kim, Point defect passivated MoS2 nanosheet based high performance piezoelectric nanogenerator, *Adv. Mater.* 30 (2018) 971–979.
- [21] A. Li, H. Pang, P. Li, N. Zhang, G. Chen, X.G. Meng, M. Liu, X.H. Liu, R.Z. Ma, J. H. Ye, Insights into the critical dual-effect of acid treatment on ZnxCd1-xS for enhanced photocatalytic production of syngas under visible light, *Appl. Catal. B Environ.* 288 (2021) 10–19.
- [22] A. Kumar, V. Krishnan, Vacancy engineering in semiconductor photocatalysts: implications in hydrogen evolution and nitrogen fixation applications, *Adv. Funct. Mater.* 31 (2021) 2009807–2009841.
- [23] Y.L. Zi, L. Lin, J. Wang, S.H. Wang, J. Chen, X. Fan, P.K. Yang, F. Yi, Z.L. Wang, Triboelectric pyroelectric piezoelectric hybrid cell for high efficiency energy harvesting and self powered sensing, *Adv. Mater.* 27 (2015) 2340–2347.
- [24] Z.B. Yang, S.X. Zhou, J. Zu, D. Inman, High performance piezoelectric energy harvesters and their applications, *Joule* 2 (2018) 642–697.
- [25] H. Yan, Z.X. Feng, S.L. Shang, X.N. Wang, Z.X. Hu, J.H. Wang, Z.W. Zhu, H. Wang, Z.H. Chen, H. Hua, A piezoelectric, strain-controlled antiferromagnetic memory insensitive to magnetic fields, *Nat. Nanotechnol.* 14 (2019) 131–138.
- [26] C.J. Shuai, G.F. Liu, Y.W. Yang, W.J. Yang, C.X. He, G.Y. Wang, Z. Liu, F.W. Qi, S. P. Peng, Functionalized BaTiO3 enhances piezoelectric effect towards cell response of bone scaffold, *Colloid Surf. B* 185 (2020), 110587, 1028–1013.
- [27] A.B. Djuricic, X.Y. Chen, Y.H. Leung, A.M.C. Ng, ZnO nanostructures: growth, properties and applications, *J. Mater. Chem.* 22 (2012) 6526–6535.
- [28] M.Y. Zhang, Q.Y. Hu, K.W. Ma, Y. Ding, C. Li, Pyroelectric effect in CdS nanorods decorated with a molecular Co-catalyst for hydrogen evolution, *Nano Energy* 73 (2020) 104810–104817.
- [29] J.D. Feng, M. Graf, K. Liu, D. Ovchinnikov, D. Dumcenco, M. Heiranian, V. Nandigana, N.R. Aluru, A. Kis, A. Radenovic, Single-layer MoS2 nanopores as nanopower generators, *Nature* 536 (2016) 197–205.
- [30] J.L. Wang, S.X. Zhou, Z.E. Zhang, D. Yurchenko, High-performance piezoelectric wind energy harvester with Y-shaped attachments, *Energy Conv. Manag.* 181 (2019) 645–652.
- [31] H.D. Li, C. Tian, Z.D. Deng, Energy harvesting from low frequency applications using piezoelectric materials, *Appl. Phys. Rev.* 1 (2014) 20–28.
- [32] Y.S. Li, E. Pan, Static bending and free vibration of a functionally graded piezoelectric microplate based on the modified couple-stress theory, *Int. J. Eng. Sci.* 97 (2015) 40–59.
- [33] M. Acosta, N. Novak, V. Rojas, S. Patel, R. Vaish, J. Koruza, G.A. Rossetti, J. Rodel, BaTiO3-based piezoelectrics: fundamentals, current status, and perspectives, *Appl. Phys. Rev.* 4 (2017) 53–62.
- [34] W.L. Deng, T. Yang, L. Jin, C. Yan, H.C. Huang, X. Chu, Z.X. Wang, D. Xiong, G. Tian, Y.Y. Gao, H.T. Zhang, W.Q. Yang, Cowpea-structured PVDF/ZnO nanofibers based flexible self-powered piezoelectric bending motion sensor towards remote control of gestures, *Nano Energy* 55 (2019) 516–525.
- [35] C.J. Shuai, Z.C. Zeng, Y.W. Yang, F.W. Qi, S.P. Peng, W.J. Yang, C.X. He, G. Y. Wang, G.W. Qian, Graphene oxide assists polyvinylidene fluoride scaffold to reconstruct electrical microenvironment of bone tissue, *Mater. Des.* 190 (2020) 108564–108571.
- [36] X. Yin, W. Wu, F.S. Zhang, L. Li, J.H. Kou, C.H. Lu, Synergistic effect of piezoelectricity and heterojunction on photocatalytic performance, *J. Photochem. Photobiol. A* 400 (2020) 112661–112669.
- [37] Z.Q. Gao, K.Y. Chen, L. Wang, B. Bai, H. Liu, Q.Z. Wang, Aminated flower-like ZnIn2S4 coupled with benzoic acid modified g-C3N4 nanosheets via covalent bonds for ameliorated photocatalytic hydrogen generation, *Appl. Catal. B Environ.* 268 (2020) 118462–118470.
- [38] C. Wang, K.W. Wang, Y.B. Feng, C. Li, X.Y. Zhou, L.Y. Gan, Y. Feng, H.J. Zhou, B. Zhang, X.L. Qu, Co and Pt dual-single-atoms with oxygen-coordinated Co-O-Pt dimer sites for ultrahigh photocatalytic hydrogen evolution efficiency, *Adv. Mater.* 33 (2021) 2003327–2003332.
- [39] M. Li, J.X. Sun, G. Chen, S.Y. Yao, B.W. Cong, P.F. Liu, Construction photothermal/pyroelectric property of hollow FeS2/Bi2S3 nanostructure with enhanced full spectrum photocatalytic activity, *Appl. Catal. B Environ.* 298 (2021) 120573–120579.
- [40] Y.F. Feng, Q.H. Deng, C. Peng, J.B. Hu, Y.D. Li, Q. Wu, Z.C. Xu, An ultrahigh discharged energy density achieved in an inhomogeneous PVDF dielectric composite filled with 2D MXene nanosheets via interface engineering, *J. Mater. Chem. C* 6 (2018) 13283–13292.
- [41] Y.L. Qiu, Z.P. Xing, M.J. Guo, Z.Z. Li, N. Wang, W. Zhou, Hollow cubic Cu2-xS/Fe-POMs/AgVO3 dual Z-scheme heterojunctions with wide-spectrum response and enhanced photothermal and photocatalytic-fenton performance, *Appl. Catal. B Environ.* 298 (2021) 120628–120635.
- [42] S.Q. Zhang, X. Liu, C.B. Liu, S.L. Luo, L.L. Wang, T. Cai, Y.X. Zeng, J.L. Yuan, W. Y. Dong, Y. Pei, Y.T. Liu, MoS2 quantum dot growth induced by S vacancies in a

ZnIn<sub>2</sub>S<sub>4</sub> monolayer: atomic level heterostructure for photocatalytic hydrogen production, *ACS Nano* 12 (2018) 751–758.

[43] S.B. Wang, Y. Wang, S.L. Zhang, S.Q. Zang, X.W. Lou, Supporting ultrathin ZnIn<sub>2</sub>S<sub>4</sub> nanosheets on Co/N-doped graphitic carbon nanocages for efficient photocatalytic H<sub>2</sub> generation, *Adv. Mater.* 31 (2019) 1347–1353.

[44] S. Luo, F. Qin, Y. Ming, H.P. Zhao, Y.L. Liu, R. Chen, Fabrication uniform hollow Bi<sub>2</sub>S<sub>3</sub> nanospheres via kirkendall effect for photocatalytic reduction of Cr(VI) in electroplating industry wastewater, *J. Hazard. Mater.* 340 (2017) 253–262.

[45] P.F. Yue, H.D. She, L. Zhang, B. Niu, R. Lian, J.W. Huang, L. Wang, Q.Z. Wang, Super-hydrophilic CoAl-LDH on BiVO<sub>4</sub> for enhanced photoelectrochemical water oxidation activity, *Appl. Catal. B Environ.* 286 (2021) 119875–119884.

[46] L. Li, Z.D. Qin, L. Ries, S. Hong, T. Michel, J. Yang, C. Salameh, M. Bechelany, P. Miele, D. Kaplan, M. Chhowalla, D. Voiry, Role of sulfur vacancies and undercoordinated Mo regions in MoS<sub>2</sub> nanosheets toward the evolution of hydrogen, *ACS Nano* 13 (2019) 6824–6834.

[47] A. Mayeen, M.S. Kala, S. Sunija, D. Rouxel, R.N. Bhowmik, S. Thomas, N. Kalarikkal, Flexible dopamine-functionalized BaTiO<sub>3</sub>/BaTiZrO<sub>3</sub>/BaZrO<sub>3</sub>-PVDF ferroelectric nanofibers for electrical energy storage, *J. Alloy. Compd.* 837 (2020) 155492–155499.

[48] W. Wang, H.S. Sun, Effect of different forms of nano-ZnO on the properties of PVDF/ZnO hybrid membranes, *J. Appl. Polym. Sci.* 137 (2020) 1–14.

[49] S.W. Han, D. Chen, J. Wang, Z. Liu, F. Liu, Y.K. Chen, Y.C. Ji, J.B. Pang, H. Liu, J. G. Wang, Assembling Sn<sub>3</sub>O<sub>4</sub> nanostructures on a hydrophobic PVDF film through metal-F coordination to construct a piezotronic effect-enhanced Sn<sub>3</sub>O<sub>4</sub>/PVDF hybrid photocatalyst, *Nano Energy* 72 (2020) 1937–1943.

[50] Q.Q. Li, W.Y. Ke, T.X. Chang, Z. Hu, A molecular ferroelectrics induced electroactive -phase in solution processed PVDF films for flexible piezoelectric sensors, *J. Mater. Chem. C* 7 (2019) 1532–1543.

[51] E. Lee, Y. Eom, Y.E. Shin, S.H. Hwang, H.H. Ko, H.G. Chae, Effect of interfacial interaction on the conformational variation of polyvinylidene fluoride chains in PVDF/graphene oxide (GO) nanocomposite fibers and corresponding mechanical properties, *ACS Appl. Mater. Interfaces* 11 (2019) 13665–13675.

[52] Q. Zhang, J.H. Zhang, X.H. Wang, L.F. Li, W.L. Dai, In-N-In sites boosting interfacial charge transfer in carbon-coated hollow tubular In<sub>2</sub>O<sub>3</sub>/ZnIn<sub>2</sub>S<sub>4</sub> heterostructure derived from In-MOF for enhanced photocatalytic hydrogen evolution, *ACS Catal.* 11 (2021) 6276–6289.

[53] Q. Zhang, H. Gu, X. Wang, L. Li, J. Zhang, H. Zhang, Y.F. Li, W.L. Dai, Robust hollow tubular ZnIn<sub>2</sub>S<sub>4</sub> modified with embedded metal-organic-framework-layers: extraordinarily high photocatalytic hydrogen evolution activity under simulated and real sunlight irradiation, *Appl. Catal. B Environ.* 298 (2021) 120632–120640.

[54] T.W. Kim, K.S. Choi, Nanoporous BiVO<sub>4</sub> photoanodes with dual-layer oxygen evolution catalysts for solar water splitting, *Science* 343 (2014) 990–994.

[55] P. Zhang, L.J. Wu, W.G. Pan, S.C. Bai, R.T. Guo, Efficient photocatalytic H<sub>2</sub> evolution over NiS-PCN Z-scheme composites via dual charge transfer pathways, *Appl. Catal. B Environ.* 289 (2021) 140–148.

[56] L.M. Guo, C.F. Zhong, J.Q. Cao, Y.N. Hao, M. Lei, K. Bi, Q.J. Sun, Z.L. Wang, Enhanced photocatalytic H<sub>2</sub> evolution by plasmonic and piezotronic effects based on periodic Al/BaTiO<sub>3</sub> heterostructures, *Nano Energy* 62 (2019) 513–520.

[57] X.F. Zhou, F. Yan, S.H. Wu, B. Shen, H.R. Zeng, J.W. Zhai, Remarkable piezophoto coupling catalysis behavior of BiO<sub>x</sub>/BaTiO<sub>3</sub> (x= Cl, Br, Cl<sub>0.166</sub>Br<sub>0.834</sub>) piezoelectric composites, *Small* 16 (2020) 15765–15772.

[58] X. Ma, G. Wang, L. Qin, J. Liu, B. Li, Y. Hu, H. Cheng, Z-scheme g-C<sub>3</sub>N<sub>4</sub>-AQ-MoO<sub>3</sub> photocatalyst with unique electron transfer channel and large reduction area for enhanced sunlight photocatalytic hydrogen production, *Appl. Catal. B Environ.* 288 (2021) 120025–120032.

[59] T. Takata, J.Z. Jiang, M. Nakabayashi, N. Shibata, V. Nandal, K. Seki, T. Hisatomi, K. Domen, Photocatalytic water splitting with a quantum efficiency of almost unity, *Nature* 581 (2020) 411–414.

[60] J. Yuan, X.Y. Huang, L.L. Zhang, F. Gao, R. Lei, C.K. Jiang, W.H. Feng, P. Liu, Tuning piezoelectric field for optimizing the coupling effect of piezo-photocatalysis, *Appl. Catal. B Environ.* 278 (2020) 119291–119299.

[61] M.Y. Wang, Y.P. Zuo, J.L. Wang, Y. Wang, X.P. Shen, B.C. Qiu, L.J. Cai, F.C. Zhou, S.P. Lau, Y. Chai, Remarkably enhanced hydrogen generation of organolead halide perovskites via piezocatalysis and photocatalysis, *Adv. Energy Mater.* 9 (2019) 190801–190808.